Title: A unique interplay of access and selection shapes peritoneal metastasis evolution in colorectal cancer

Authors:

Emma CE Wassenaar[1,2,*], Alexander N Gorelick[3,4,*], Wei-Ting Hung[4,15], David M Cheek[3,4], Emre Kucukkose[2], I-Hsiu Lee[3,4], Martin Blohmer[3,4,5], Sebastian Degner[3,4], Peter Giunta[3,4], Rene MJ Wiezer[1], Mihaela G Raicu[6,7], Inge Ubink[2], Sjoerd J Klaasen[7], Nico Lansu[7], Emma V. Watson[8], Ryan B. Corcoran[9], Genevieve Boland[10,11], Gad Getz[11,12,13], Geert JPL Kops[7], Dejan Juric[11,14], Jochen K Lennerz[13], Djamila Boerma[1], Onno Kranenburg[2], Kamila Naxerova[3,4,#]

Affiliations:
[1]Department of Surgery, St. Antonius Hospital, Nieuwegein, the Netherlands
[2]Department of Surgical Oncology, Laboratory Translational Oncology, University Medical Center Utrecht, Utrecht, the Netherlands
[3]Department of Genetics, Harvard Medical School, Boston, MA, USA;
[4]Center for Systems Biology, Massachusetts General Hospital Research Institute and Harvard Medical School, Boston, MA, USA;
[5]Charité - Universitätsmedizin Berlin, Berlin, Germany;
[6]Department of Pathology, St. Antonius Hospital, Nieuwegein, the Netherlands
[7]Oncode Institute, Hubrecht Institute-KNAW (Royal Academy of Arts and Sciences) and University Medical Centre Utrecht, Utrecht, the Netherlands
[8]University of Massachusetts Medical School, Worcester, MA, USA
[9]Division of Hematology and Oncology, Department of Medicine, Massachusetts General Hospital Cancer Center, Harvard Medical School, Boston, MA, USA
[10]Division of Surgical Oncology, Department of Surgery, Massachusetts General Hospital Cancer Center, Harvard Medical School, Boston, MA, USA
[11]Krantz Family Center for Cancer Research, Massachusetts General Hospital, Boston, MA, USA
[12]Cancer Program, Broad Institute of MIT and Harvard, Cambridge, MA, USA
[13]Department of Pathology, Massachusetts General Hospital, Boston, MA, USA
[14]Termeer Center for Targeted Therapies, Massachusetts General Hospital, Boston, MA, USA
[15]Present address: Graduate Institute of Medical Genomics and Proteomics, National Taiwan University, Taipei, Taiwan;

[*]These authors contributed equally.

[#]**Correspondence to:**

Kamila Naxerova
77 Avenue Louis Pasteur, NRB 239F
Boston, MA 02115, USA
kamila_naxerova@hms.harvard.edu

1   Abstract

2

3   Whether metastasis in humans can be accomplished by most primary tumor cells or requires the

4   evolution of a specialized trait remains an open question. To evaluate whether metastases are

5   founded by non-random subsets of primary tumor lineages requires extensive, difficult-to-

6   implement sampling. We have realized an unusually dense multi-region sampling scheme in a

7   cohort of 26 colorectal cancer patients with peritoneal metastases, reconstructing the evolutionary

8   history of on average 28.8 tissue samples per patient with a microsatellite-based fingerprinting

9   assay. To assess metastatic randomness, we evaluate inter- and intra-metastatic heterogeneity

10   relative to the primary tumor and find that peritoneal metastases are more heterogeneous than liver

11   metastases but less diverse than locoregional metastases. Metachronous peritoneal metastases

12   exposed to systemic chemotherapy show significantly higher inter-lesion diversity than

13   synchronous, untreated metastases. Projection of peritoneal metastasis origins onto a spatial map

14   of the primary tumor reveals that they often originate at the deep-invading edge, in contrast to liver

15   and lymph node metastases which exhibit no such preference. Furthermore, peritoneal metastases

16   typically do not share a common subclonal origin with distant metastases in more remote organs.

17   Synthesizing these insights into an evolutionary portrait of peritoneal metastases, we conclude that

18   the peritoneal-metastatic process imposes milder selective pressures onto disseminating cancer

19   cells than the liver-metastatic process. Peritoneal metastases' unique evolutionary features have

20   potential implications for staging and treatment.

Introduction

The life history of metastases in humans remains poorly understood. Although recent advances in multi-region sequencing have uncovered important new insights into the dynamics of metastasis formation[1–5], many foundational questions remain unanswered. One prominent unresolved question concerns the distribution of metastatic potential among primary tumor cells. Are all primary tumor cells similarly likely to become metastasis founder cells? Or do lineages with superior ability to execute at least one of the steps of the metastatic cascade exist[6]? Clonal lineages with variable, mitotically heritable metastatic potential have been demonstrated in mice[7,8]. In human cancer, the situation is less clear, as it has been challenging to identify molecular features that are enriched in metastases over primary tumors[9,10]. A principled search for possible molecular promoters of metastasis (mutations, copy number variants, epigenetic alternations, heritable changes in gene expression) would be greatly enabled if we could ascertain whether human metastases descend from cells with specialized attributes.

If metastases are in fact derived from cells that have acquired specialized pro-metastatic traits, then we would expect them to represent a non-random sample of primary tumor lineages. Conversely, if no specialized trait is required, all primary tumor subclones will be equally likely to give rise to metastases. To test the null hypothesis of metastatic randomness, two elements are required: a detailed picture of the clonal diversity in the primary tumor, and the genotypes of as many distinct metastases from the same patient as possible. If only a single metastasis is analyzed, it is difficult to judge whether the lesion was seeded by a lineage with increased metastatic capacity or whether it originated from a disseminated cell that managed to grow out by chance. If, on the other hand, multiple analyzed metastases all belong to the same lineage, we may suspect with greater confidence that some functional specialization has occurred.

Arguably the greatest hurdle for the study of metastatic randomness is the extreme difficulty of obtaining suitable tissue samples. Metastases are rarely surgically resected. Research autopsies represent valuable opportunities for metastasis collection, but the primary tumor has often been removed at the time of death and may not be available. Obtaining multi-region sampled primary tumors and matched metastases through prospective collection is a daunting task due to the rarity

52 of such cases. Retrospective collection of formalin-fixed and paraffin-embedded (FFPE) samples

53 is more feasible, but it can be technically challenging to work with these specimens, and a patient's

54 consent to broad sequencing – which exposes germline variants that in conjunction with other data

55 types can be used to identify individuals[11] – may not be available years after the fact.

56

57 Together, these challenges have resulted in a paucity of data that could effectively illuminate the

58 question of metastatic randomness. We have previously circumnavigated some of these problems

59 by reconstructing the evolutionary history of metastatic cancers with a scalable microsatellite

60 fingerprinting assay that is suitable for archival FFPE samples[12–15]. Applying the method to a large

61 cohort of patients with metastatic colorectal cancer, we made a surprising discovery: we found that

62 liver metastases showed strong evidence of non-randomness, usually arising from a small subset

63 of the lineages that were detected in the primary tumor[14]. In contrast, lymph node metastases were

64 sampled from the primary tumor much more randomly. These results suggested that the

65 evolutionary rules of metastasis formation differ from host organ to host organ. Liver metastases

66 are formed by a privileged subset of primary tumor lineages, likely because the liver-metastatic

67 process imposes severe selective constraints onto disseminating tumor cells, restricting successful

68 colonization to only a few subclones with heritably increased liver-metastatic potential. Other

69 environments, like the lymphatic system, seem to represent a friendlier milieu[16,17] that can be

70 successfully navigated by a larger fraction of primary tumor cells.

71

72 Here we investigate the host organ-specific properties of colorectal cancer metastases in one of the

73 most important but largely overlooked sites: the peritoneum. Peritoneal metastasis is frequent –

74 5.7% of colon cancer patients have peritoneal metastases at the time of diagnosis, and 5.5% more

75 will develop them in the course of their disease[18], making the peritoneum the most frequent site of

76 distant metastasis after the liver. Peritoneal metastasis patients have a poor prognosis; even if the

77 peritoneum is the only affected site, median survival is a mere 16 months[19]. Despite its frequency,

78 very little is known about the genetics of peritoneal disease in colorectal cancer, and new insights

79 that could ultimately guide more effective treatment strategies are needed. Few comprehensive

80 studies have examined this disease entity, and existing data are mostly gene expression-

81 focused[20,21]. Not only do we not know to what degree peritoneal metastasis is non-random, we also

82 do not know where peritoneal metastases originate and what their relationship to other locoregional

83 and distant metastases is. This study aims to address these questions by leveraging a unique patient

84 cohort with multi-region sampled primary tumors and matched peritoneal metastases.

85 **Results**

86

87 *Polyguanine fingerprints reconstruct the evolutionary history of metastatic cancers*

88 To study the evolution of peritoneal metastasis in human colorectal cancer patients, we assembled

89 a retrospective cohort suitable for high density multi-region sampling. To be included in the study,

90 patients had to be diagnosed with colorectal adenocarcinoma, and FFPE resection specimens of

91 the primary tumor and at least one (but ideally multiple, spatially distinct) peritoneal metastases

92 had to be available. For all patients that met these criteria (*n*=24, detailed clinical information in

93 **Supplementary Table 1**), we made every effort to sample *all* surgically resected cancer

94 components as comprehensively as possible. This approach resulted in dense sample coverage: on

95 average, we successfully analyzed 28.8 tissue samples per patient (9.1 primary tumor areas, 10.5

96 peritoneal lesions, 5.2 locoregional metastases, 3.0 non-peritoneal distant metastases, and one

97 normal tissue control, **Fig. 1a**, sample information in **Supplementary Table 2**). All but two

98 patients had multiple peritoneal metastases. Within the constraints imposed by their specific

99 characteristics (e.g. stromal content), we sampled primary tumors proportionately to their size

100 (**Supplementary Figure 1**). We also acquired high-resolution images of hematoxylin and eosin

101 (H&E) stained sections of all 445 FFPE tissue blocks from these patients, providing detailed

102 microanatomical maps for all samples. We supplemented the cohort with two previously analyzed

103 patients with multi-region sampled primary tumors and multiple peritoneal metastases (C38,

104 C89).[13,14]

105

106 To reconstruct the evolutionary history of each patient's cancer, we used polyguanine

107 fingerprinting, a somatic lineage tracing method that relies on detection of insertion and deletion

108 mutations in polyguanine microsatellites[12–15]. Polyguanine repeats mutate at very high rates ($\mu \approx$

109 10^{-4} per division per allele[15]) and thus act as natural molecular 'barcodes' that record a somatic

110 lineage's history with high efficiency. In colorectal cancer, interrogation of merely a few dozen

111 tracts is typically sufficient to generate statistically well-supported phylogenetic trees that

112 represent the lineage relationships between the cell populations in each sample[13]. Polyguanine
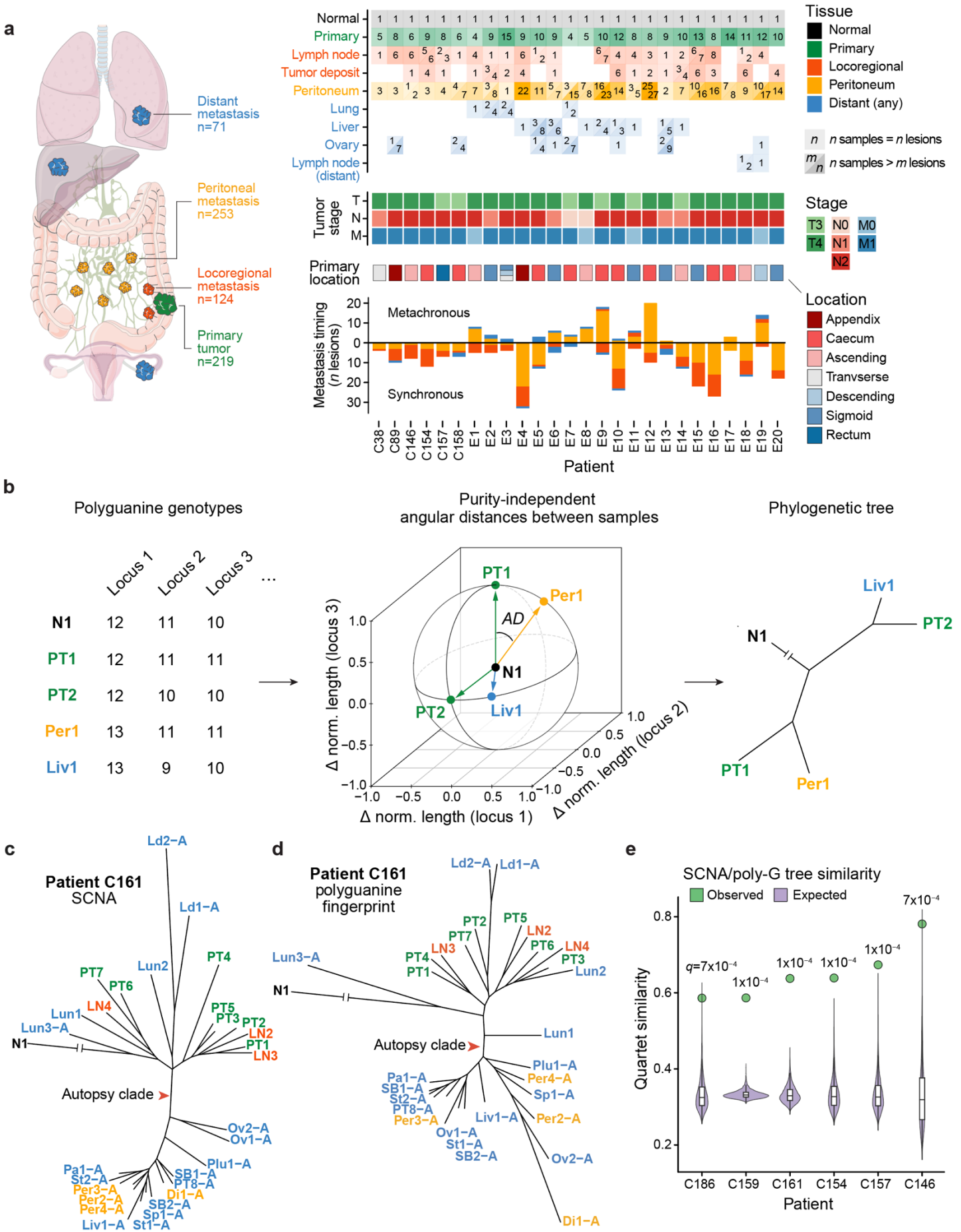
Figure 1. Polyguanine fingerprints reconstruct cancer evolution. a, Patient cohort overview. *Left*, Types and total numbers of samples analyzed in this study. *Right*, Overview of samples analyzed per patient, as well as AJCC Tumor, Node, and Metastasis (TNM) staging at diagnosis, primary tumor location, number of analyzed synchronous and metachronous metastatic lesions. **b,** Reconstruction of tumor evolution from polyguanine fingerprints. Each tumor sample is genotyped at approximately 31 polyguanine loci (here, only three are shown for simplicity). Polyguanine fingerprints are created by subtracting the germline genotype from each tumor sample's vector of mean polyguanine lengths. The angular distance (*AD*) between two unit length-normalized polyguanine fingerprints (e.g. PT1 and Per1) is defined as $\arccos(PT1 \cdot Per1)$. Phylogenetic trees are built from angular distance matrices with the neighbor-joining algorithm. The normal tissue sample is attached post hoc to the last internal node created. **c-d,** Comparison of phylogenetic trees reconstructed from somatic copy number alterations (SCNAs) **(c)** or polyguanine fingerprints **(d)** for patient C161. *PT*, primary tumor; *LN*, lymph node metastasis; *Per*, peritoneal metastasis; *Liv*, liver metastasis; *Lun*, lung metastasis; *Ld*, distant lymph node metastasis; *Di*, diaphragm metastasis; *Ov*, ovarian metastasis; *Pa*, pancreas metastasis; *Plu*, pleural metastasis; *SB*, small bowel metastasis; *Sp*, splenic metastasis; *St*, stomach metastasis. **e,** Quartet similarity between polyguanine and SCNA-based phylogenetic trees for 6 patients. *Green*, observed similarity. *Purple*, similarity expected by chance based on 1,000 random permutations of tree tip labels. Permutation-based *p*-values corrected for multiple-hypothesis testing by Holm's method (*q*-values).

113   fingerprints are generated by multiplex PCR and fragment analysis without the need for

114   sequencing, providing several important advantages: first, the simplicity of the method allows it

115   to perform robustly even on partially degraded DNA from older clinical FFPE specimens. Second,

116   a research participant's identity cannot be inferred from the data since no single nucleotide

117   polymorphisms are captured, and no population databases of polyguanine sequences exist. These

118   properties allow us to apply polyguanine fingerprinting to archival clinical samples that are

119   typically off limits to other genetic analysis methods.

120

121   A disadvantage of polyguanine fingerprints is that precise tumor purity is difficult to estimate from

122   the data. Prior studies using the methodology therefore had to be restricted to (manually

123   macrodissected) samples of high purity[12–14]. This approach was not feasible for peritoneal

124   metastases, which are often diffusely infiltrated with stromal cells[22]. To enable accurate

125   phylogenetic reconstruction from samples of variable purity, we developed a purity-robust genetic

126   distance. It takes advantage of the fact that the *direction* of a cancer sample's polyguanine

127   fingerprint (defined as the vector of mean allele lengths for all loci, minus the patient-matched

128   germline genotype) is independent of tumor purity, although its magnitude is not. We therefore

129   use the angle between two cancer sample's polyguanine fingerprints (the "angular distance") as a

130   purity-independent measure of genetic divergence (**Fig. 1b**). In a **Supplementary Note**, we offer

131   a detailed mathematical explanation of the angular distance in the context of a random walk model

132   of polyguanine evolution, show simulations to confirm that the angular distance between two

133   tumors with purities greater than 15% approximates the angular distance under optimal conditions

134   (*i.e.*, 100% purity in each tumor) and provide additional details regarding phylogenetic

135   reconstruction, including post-hoc attachment of the normal tissue root.

136

137   With the new, purity-robust angular distance integrated into our existing analysis pipeline, which

138   involves extensive quality control, minimum purity filtering, and normalization of polyguanine

139   fingerprints[13,14] (**Methods**), we next sought to validate the new approach. We collected 30 spatially

140   and temporally distinct samples from a patient with metastatic colorectal cancer, comprising the

141   primary tumor and its associated locoregional lymph node metastases, two surgically resected lung

142   metastases, as well as 19 samples from widely disseminated disease at the time of death (labeled

143   with suffix -A in **Fig. 1c**). We performed low-pass whole genome sequencing (lpWGS, ~1x depth

144   of coverage) of all samples and used the resulting data to estimate tumor purity and call somatic

145   copy number alterations (SCNAs) (**Methods**). As expected, purity was variable and ranged

146   between 0.16 and 0.44 (**Supplementary Table 3**). A phylogeny constructed based on purity-

147   corrected SCNA profiles showed an informative topology (**Fig. 1c**): the primary tumor diversified

148   early and locoregional lymph node metastases resembled it closely, a pattern we have described

149   previously[14,15]. Two lung metastases that were resected while the patient was still alive clustered

150   with the primary tumor as well. In contrast, almost all metastases collected at rapid autopsy –

151   except for lung metastasis Lun3-A and distant lymph node metastases Ld1-A and Ld2-A – formed

152   a distinct, homogeneous clade, indicating that widely disseminated disease at the time of death

153   was the result of a recent clonal expansion. The phylogeny based on angular distances among

154   polyguanine fingerprints recovered the same main features (**Fig. 1d**). The trees agreed on all major

155   points, including the significant difference between the primary tumor and most autopsy

156   specimens, the clustering of locoregional metastases with the primary, and the separation of Ld1/2-

157   A and Lun3-A from the rest of the autopsy samples. One difference was a closer relationship

158   between lung metastasis Lun1 and the autopsy sample clade in the polyguanine tree. A comparison

159   of the two phylogenies using quartet similarity, a widely used measure of tree resemblance[23],

160   showed highly significant concordance ($p<1x10^{-4}$, see **Methods** for details). To establish

161   generality, we repeated the comparison between trees constructed from lpWGS-derived SCNAs

162   and polyguanine fingerprinting for five more patients and 119 samples of variable purity

163   (**Supplementary Table 3**) and observed the same high level of reproducibility in all cases

164   (summary in **Fig. 1e**, all polyguanine- and SCNA-based phylogenies are shown in **Supplementary**

165   **Fig. 2**). Overall, these data suggest that angular distance trees handle purity differences adequately

166   and provide robust phylogenetic information.

167

168   ***Peritoneal metastases are genetically more diverse than liver metastases***

169   We reconstructed angular distance-based phylogenies for all patients in the peritoneal metastasis

170   cohort and examined their topologies (**Supplementary Fig. 3**). The first question we hoped to

171   answer concerned metastatic randomness. Do anatomically distinct peritoneal metastases

172   generally resemble each other more than they resemble the primary tumor (low inter-metastatic

173   diversity, **Fig. 2a**)? Or are their genotypes divergent, matching different primary tumor areas more

174   than each other (high inter-metastatic diversity, **Fig. 2b**)? The first scenario would be indicative of

9
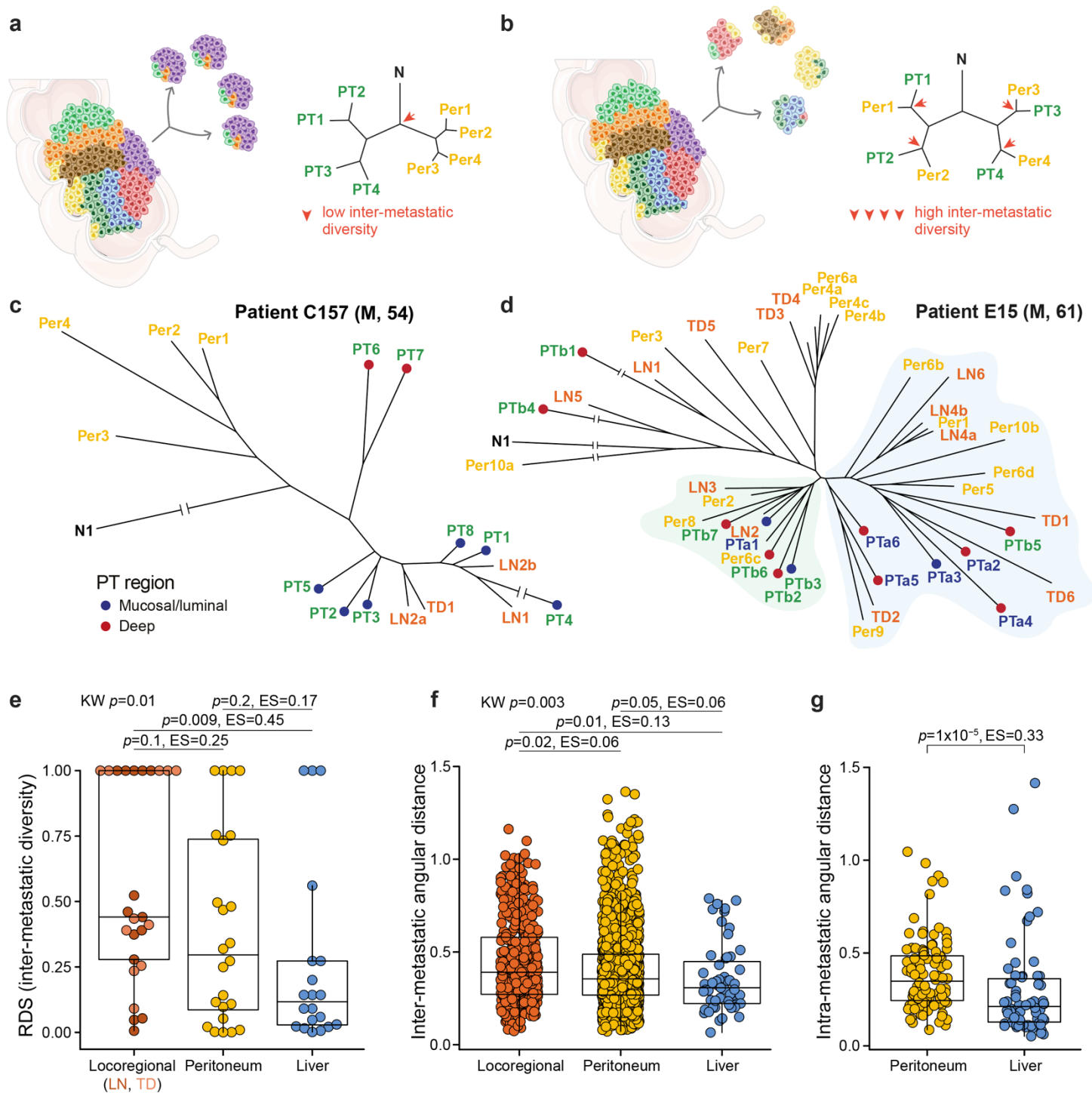
Figure 2. Peritoneal metastases exhibit intermediate inter-metastatic diversity. a-b, Schematic illustrating low **(a)** or high **(b)** inter-metastatic diversity in two hypothetical patients. Colored cells represent distinct lineages originating in the primary tumor. **c-d,** Phylogenetic trees for patients C157 and E15, illustrating low **(c)** and high **(d)** inter-metastatic diversity of peritoneal lesions. *Td*, tumor deposit; all other sample type abbreviations as in Figure 1. Spatial localization of primary tumor samples (deep-invasive or mucosal/luminal) is indicated in blue and red. In **(d),** clades enriched for two spatially distinct primary tumors Pta and PTb are shaded in blue and green,

10

respectively. **e,** Metastasis-specific root diversity scores (RDS) for locoregional, peritoneal, and liver metastases. Each point represents a patient. Lymph node metastases and tumor deposits are evaluated separately but plotted together as locoregional metastases. Kruskal-Wallace *p*-value is shown, along with Dunn's test *p*-values for each pairwise comparison with Holm's correction for multiple hypothesis testing. Effect sizes are based on Wilcoxon Rank Sum tests run independently for each pairwise comparison. **f,** Comparison of inter-metastatic diversity by pairwise angular distances. Each point is the angular distance between a pair of distinct metastatic lesions of the indicated type within a patient. Values in the locoregional category include all pairwise distances between lymph node metastases and tumor deposits. *P*-values and effect sizes as in **(c)**. **g,** Comparison of *intra*-metastatic diversity quantified by pairwise angular distances. Each point is the angular distance between a pair of spatially distinct samples taken from the same metastatic lesion. Only metastatic lesions with 2 or more sampled region are included. Wilcoxon rank sum test *p*-value and effect size.

175   peritoneal metastasis formation by only one (or a small subset) of the lineages that are present in

176   the primary tumor, while the second scenario would be consistent with many different primary

177   tumor subclones colonizing the peritoneum in parallel. If only a small number of subclones

178   contributes to peritoneal disease, we can conclude that either access to the peritoneal cavity must

179   be restricted to limited portions of the primary tumor, or that stringent selection prevents the

180   outgrowth of all but a few (specialized) lineages.

181

182   Inspecting tumor phylogenies, we found examples of both high and low inter-metastatic

183   heterogeneity in the peritoneum. For example, four synchronous, spatially distinct peritoneal

184   metastases (Per1-4, located in the omentum and hemidiaphragm) from patient C157 had a recent

185   common ancestor that clearly segregated away from the primary tumor and its associated

186   locoregional lymph node metastases (**Fig. 2c**). The tree topology indicated that all peritoneal

187   metastases had a relatively similar genetic composition and had descended from lineages that were

188   not readily detectable in the primary tumor. Patient C157 was one of the few patients in our cohort

189   who had provided informed consent for broad next-generation sequencing, we could thus

190   additionally examine their cancer with lpWGS and deep whole exome sequencing. We found that

191   all three methods agreed: peritoneal metastases were enriched for a unique clonal population that

192   was not present at appreciable frequencies in any other analyzed samples (**Supplementary Figs.**

193   **2 and 4**).

194

195   In contrast, patient E15's peritoneal metastases exhibited extensive inter-metastatic heterogeneity

196   (**Fig. 2d**). Metastases in this case were also synchronous and had been resected along with two T4

197   stage primary tumors that grew 7 cm apart in the sigmoid colon. Using a recently established

198   classification methodology[15], we found that the two primaries had a common clonal origin

199   (**Supplementary Fig. 5a** shows this classification for E15 and all other patients who had more

200   than one primary tumor). Subclonal diversity in tumor PTb was significantly larger than in tumor

201   PTa (**Supplementary Fig. 5b**), indicating that it was older[24] and had likely seeded PTa, a

202   hypothesis that was also consistent with PTb's larger size (4.5 cm vs. 1.5cm for PTa). While 5 out

203   of 6 PTa samples clustered in a common clade (along with area PTb5 which might have been

204   involved in the genesis of PTa), the patient's ten peritoneal metastases were randomly distributed

205   throughout the tree, indicating that they were as clonally diverse as the two primary tumors.

206

207 To quantify inter-metastatic heterogeneity (i.e. genetic diversity between anatomically distinct

208 metastases with respect to the multi-region sampled primary tumor) across all patients, we

209 employed our previously developed 'root diversity score' (RDS) mathematical framework[14]. The

210 RDS quantifies the probability of observing monophyletic clades containing l metastases of the

211 same type on phylogenetic trees with m total metastases of that type and k other tumor samples.

212 For example, patient C157's tree contains $m=4$ peritoneal metastases and $k=12$ samples that are

213 not peritoneal metastases (8 primary tumor samples and 4 locoregional metastasis samples, **Fig.**

214 **2c)**. All peritoneal metastases form a monophyletic clade ($l=4$). The probability that this 4-out-of-

215 4 clustering of peritoneal metastases occurs by chance alone is given by the RDS and is 7.7×10^{-4}

216 in this case. Thus, low RDS values indicate that metastases are genetically homogeneous with

217 respect to the rest of the cancer, while high values indicate polyphyletic metastasis origins and

218 high inter-metastatic diversity. Here, we calculated RDS values in a metastasis-specific manner:

219 we constructed trees with only samples from the primary tumor and the metastasis type under

220 investigation and compared the cohort-wide RDS distributions for locoregional, peritoneal and

221 liver metastases (see **Methods** for more details, **Supplementary Table 5** for all metastasis-specific

222 RDS values). Since few individuals in the this study had liver metastases (their presence was not

223 among the selection criteria), we included data from 30 previously published[13,14] liver metastasis

224 patients in this analysis.

225

226 We observed that locoregional metastases – encompassing lymph node metastases and tumor

227 deposits – were genetically diverse (high RDS values), while liver metastases were more

228 homogeneous (low RDS values, **Fig. 2e**), as we had previously noted[14]. Peritoneal metastasis RDS

229 values fell in-between, indicating intermediate diversity in the peritoneum. We obtained the same

230 result when comparing pairwise inter-lesion angular distances between locoregional, peritoneal

231 and liver metastases (**Fig. 2f**). Leveraging a considerable number of multi-region sampled

232 metastatic lesions, we also compared *intra*-lesion angular distances between peritoneal and liver

233 metastases and found that peritoneal metastases also contained greater clonal diversity *within*

234 individual lesions (**Fig. 2g**). Although peritoneal metastasis is clinically viewed as a form of distant

235 metastasis (defining stage IV disease), its progression mechanism has long been suspected to be

236 more of a locoregional nature, potentially involving direct seeding through breaches in the serosal

13

237   membrane[25,26]. It is therefore noteworthy that broadly, genetic diversity among peritoneal

238   metastases is intermediate compared with locoregional and 'true distant' liver metastases,

239   potentially indicating that seeding to farther organs imposes more severe selective pressures and

240   thus reduces genetic heterogeneity.

241

242   ***Genetic diversity is increased among metachronous peritoneal metastases exposed to systemic***

243   ***chemotherapy***

244   Next, we wanted to dissect the possible influence of clinical history and treatment on genetic

245   diversity across the different metastasis types. We had previously found that the stark disparity in

246   inter-metastatic diversity between lymph node and liver metastases was most pronounced for

247   synchronous, untreated lesions, indicating that these differences were driven by inherent biology

248   rather than timing or treatment effects[14]. Subsetting root diversity scores to retain only

249   synchronous, untreated lesions, we again found that the RDS distributions of locoregional and

250   liver metastases remained significantly different, with no diminishment in effect size (**Fig. 3a**).

251   Root diversity scores in the peritoneal group remained in their intermediate position but shifted

252   towards lower values, prompting us to investigate explicitly whether inter-metastatic diversity in

253   the peritoneum varied as a function of clinical history.

254

255   The two main variables of interest – treatment history and metastasis timing – could not be studied

256   separately since synchronous metastases were almost always untreated and metachronous

257   metastases were almost always treated in this cohort. We did have a small number of

258   synchronous/treated or metachronous/untreated metastases, but the number of patients in these

259   categories never exceeded two, precluding meaningful statistical analysis (**Supplementary Table**

260   **4**). All subsequent comparisons therefore focus on metastases that were resected along with the

261   primary tumor and had never been exposed to any kind of treatment (labeled

262   "synchronous/untreated" from now on) and metastases that were resected in a separate surgery

263   more than three months after primary tumor resection and had experienced systemic chemotherapy

264   exposure (labeled "metachronous/treated").

265

266   Comparing inter-lesion diversity between synchronous/untreated and metachronous/treated

267   peritoneal metastases, we found large and significant differences for both RDS (**Fig. 3b**) and inter-

14
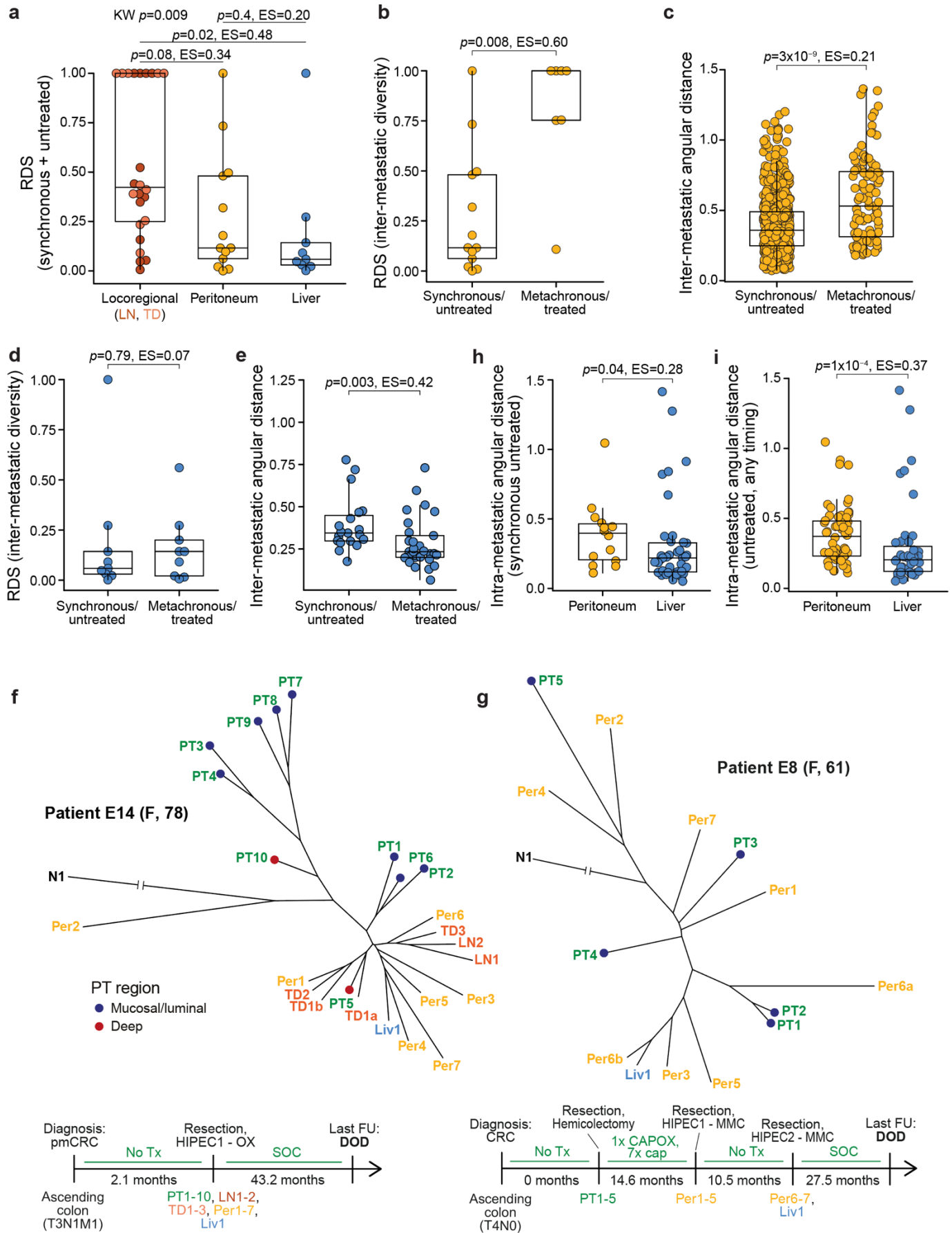
Figure 3. Inter-metastatic diversity varies by timing and treatment. a, Inter-metastatic diversity (RDS) of synchronous/untreated locoregional, peritoneal, and liver metastases. RDS calculations are based on a reduced phylogeny consisting only of the patient's primary tumor, normal tissue, and synchronous/untreated metastases of the indicated tissue type. *P*-values and effect sizes as described in Fig. 2e. **b-c,** Inter-metastatic diversity among synchronous/untreated and metachronous/treated peritoneal metastases based on RDS **(b)** and pairwise inter-lesion angular distances **(c)**. **d-e,** As in (b-c) but for liver metastases. **f,** Phylogenetic tree and clinical timeline for patient E14. pmCRC, colorectal cancer with peritoneal metastasis; OX, oxaliplatin. **g,** Phylogenetic tree and clinical timeline for patient E8. MMC, mitomycin C; CAPOX, capecitabine and oxaliplatin. **h,** Intra-metastatic diversity in synchronous/untreated peritoneal and liver metastases. Intra-metastatic diversity is quantified as in Fig. 2g. **i,** As in (h), but including all untreated peritoneal and liver metastases regardless of timing. *P*-values and effect sizes for all comparisons between two groups (b-e, h, i) are from Wilcoxon rank sum tests.

16

268   lesion angular distances (**Fig. 3c**). The effect was specific to the peritoneum, as the RDSs of

269   synchronous/untreated and metachronous/treated liver metastases were similar (**Fig. 3d**), and the

270   inter-lesion angular distances even were diminished in the treated/metachronous setting (**Fig. 3e**).

271   Locoregional metastases are almost always resected at the same time as the primary tumor, the

272   comparison could thus not be performed for these lesions.

273

274   The cohort-wide patterns summarized in **Figs. 3b-c** were easily visible on the patient level. For

275   example, the phylogenetic tree of patient E14 – whose primary tumor, locoregional metastases

276   (n=5), peritoneal metastases (n=7) and liver metastasis (n=1) were resected synchronously with no

277   neoadjuvant treatment – showed that most peritoneal metastases were closely related to each other

278   (peritoneal metastasis-specific RDS=0.1, **Fig. 3f)** and resembled primary tumor area PT5. The

279   remaining nine primary tumor regions located to other branches of the phylogenetic tree and did

280   not appear to share any direct ancestry with the peritoneal metastases. Notably, in this patient, all

281   locoregional metastases as well as the liver lesion also originated from that same metastatic

282   lineage.

283

284   In contrast, peritoneal metastases were highly diverse in patient E8 who had undergone a primary

285   tumor resection with curative intent and had then been treated with adjuvant systemic

286   chemotherapy (**Fig. 3g**). Fourteen and 25 months after the initial surgery, the patient completed

287   two cytoreductive surgeries and hyperthermic intraperitoneal chemotherapies (HIPECs) in which

288   five and two peritoneal metastases were resected, respectively. In this patient, peritoneal

289   metastases were intermixed with various primary tumor areas on the phylogenetic tree and there

290   appeared to be no distinct peritoneal-metastatic lineage. Even multiple samples from the same

291   metastatic lesion (Per6a,b) did not cluster together, indicating high degrees of subclonal diversity.

292

293   Treatment drives cancer evolution[27], potentially explaining elevated levels of inter-metastatic

294   diversity in metachronous/treated peritoneal metastases. However, we were surprised to find that

295   the presumed treatment effect was host organ-specific, as no elevated diversity could be detected

296   for metachronous/treated liver metastases. We hypothesized that this observation could be

297   explained by exacerbation of *pre-existing* clonal diversity through chemotherapy-induced cell

298   death and regrowth cycles which amplify heterogeneity via genetic drift. This reasoning is

17

299   attractive because it relies on minimal assumptions, requiring only that cancer cells die as a

300   consequence of chemotherapy. Pursuing this hypothesis, we returned to a closer examination of

301   the baseline differences that exist between peritoneal and liver metastases. Focusing exclusively

302   on lesions that were resected at the same time as the primary tumor and had not experienced any

303   kind of treatment, we found that – as for all peritoneal and liver metastases, shown in **Fig. 2g** –

304   *intra*-lesion heterogeneity was significantly higher in the peritoneum (**Fig. 3h**). The same was also

305   true for all untreated lesions regardless of timing (**Fig. 3i**). Therefore, in their 'natural' untreated

306   state, peritoneal metastases contain more intra-lesion clonal diversity than liver metastases.

307

308   We wondered whether the diversity gap between peritoneal and liver metastases was a general

309   biological property that could be recapitulated in a mouse model of colorectal cancer. We

310   transduced patient-derived organoids (PDOs) with multi-color lentiviral LeGO[28] vectors to create

311   artificial 'color lineages' that could be tracked by fluorescence microscopy. We implanted the cells

312   in the caecum of immunocompromised mice and imaged spontaneously arising peritoneal and liver

313   metastases (**Methods**). We observed high color heterogeneity within peritoneal metastases, while

314   liver metastases were mostly uniform in color (**Supplementary Fig. 6**). Unbiased quantification

315   of intra-lesion color diversity across all images via Simpson's diversity index showed significantly

316   higher diversity in the peritoneum.

317

318   Together, these data demonstrate that intra-lesion diversity is higher in the peritoneum than in the

319   liver in the untreated setting, both in the mouse and in humans. To illustrate how chemotherapy

320   might shape this baseline diversity, we considered a simple stochastic 'toy' model of cell death

321   and regrowth (**Methods**). In this model, metastases are created and populated with subclones *in*

322   *silico*. Metastases in one class are assigned high levels of intra-lesion diversity, while metastases

323   in the other class are assigned low levels (**Supplementary Fig. 7**). Chemotherapy is then simulated

324   as the random death of 80% (or 40%) of cells in each lesion. After therapy, each metastasis is

325   regenerated through a random birth-death process and intra- and inter-lesion diversity are recorded.

326   As predicted by the laws of genetic drift, we observe that chemotherapy-related death and regrowth

327   fuel inter-lesion diversification among metastases. The most dramatic increases are seen for

328   metastases that harbor more intra-lesion diversity at baseline (**Supplementary Fig. 7**), in line with

329   our experimental data. Due to the universality of the underlying principle (namely: following the

18

330 death of a fraction of cells, regrowth will invariably remodel clone frequencies through drift, with

331 the greatest absolute impact on lesions with higher baseline heterogeneity), these results are

332 qualitatively robust to large variation in all model parameters.

333

334 We conclude that repeated cycles of cell death and regrowth can exacerbate pre-existing genetic

335 heterogeneity through neutral drift. While our simple model is potentially sufficient to explain why

336 peritoneal metastases show greater post-treatment heterogeneity than liver metastases, we can of

337 course not exclude the possibility of other, more complex factors at play, such as treatment-related

338 selection that varies systematically across clones or host organs. Also, since our data cannot

339 formally clarify whether treatment or metastasis timing is responsible for the high inter-lesion

340 diversity among metachronous/treated peritoneal metastases, effects related to the timing of

341 resection should be considered as well. For example, it is possible that seeding of metachronous

342 metastases occurs by a distinct route (e.g. through release of cancer cells during surgery[29]), which

343 could affect their clonal diversity.

344

345 ***Clones on the deep-invading tumor edge are closely related to peritoneal metastases***

346 From the data presented thus far, a first evolutionary portrait of colorectal cancer peritoneal

347 metastases is emerging. In comparison with liver metastases, peritoneal metastases contain

348 relatively high levels of intra-lesion genetic diversity (**Fig. 3h-i**). However, at least in the

349 synchronous/untreated setting, anatomically distinct peritoneal metastases also tend to form

350 monophyletic clades (**Fig. 3b**), meaning that they frequently resemble each other. Taken together,

351 these two observations suggest that peritoneal metastases are typically composed of multiple

352 subclones and that these subclones are distributed across peritoneal lesions in similar proportions,

353 leading to relative uniformity *between* metastases (demonstrated for example for patient C157 in

354 **Supplementary Fig. 4**). Many phylogenies further show that most primary tumor lineages are not

355 directly related to peritoneal subclones in the synchronous/untreated setting (e.g. **Fig. 3f**).

356

357 These observations raise the question of what is special about the clones that form peritoneal

358 metastases. One possibility is that these lineages acquired a novel trait that allowed them to

359 colonize the peritoneum. Alternatively, their specialization could be of a spatial nature: they could

360 be preferentially located on the deep-invading edge of the primary tumor and have increased access

361 to the peritoneal cavity (**Fig. 4a**). Clinical data[30] demonstrate that patients with T4 stage primary

362 tumors, which by definition have breached the peritoneal lining, are particularly likely to have

363 synchronous peritoneal metastases (**Fig. 4b**). In contrast, most patients with isolated synchronous

364 liver metastases have T3 stage primary tumors. These data suggest a strong and specific association

365 between peritoneal metastasis and local invasion. However, no direct evidence for a local seeding

366 mechanism exists so far in humans. Since some extra-abdominal malignancies such as lung and

367 breast cancer also metastasize to the peritoneum[26], the possibility of hematogenous metastasis (and

368 organotropism) cannot be excluded[25]. We reasoned that our dense multi-region sampling scheme

369 might be able to pinpoint the spatial localization of peritoneal metastasis origins in the primary

370 tumor.

371

372 To determine whether deep-invading primary tumor regions were more likely to be related to

373 peritoneal metastases than luminal areas, we returned to the H&E images annotated with precise

374 sampling locations. A board-certified gastrointestinal pathologist reviewed the images and

375 classified each primary tumor sample as belonging to the "luminal" or "deep-invading" edge.

376 Several interesting observations emerged after we overlayed these annotations onto the

377 phylogenetic trees. First, we noticed that in many patients who exhibited overall clear segregation

378 of primary tumor and peritoneal metastases, a small subset of sampled primary tumor regions

379 separated from the remainder and clustered among peritoneal metastases. Without exception, such

380 'runaway' primary tumor samples were from the deep-invading edge. For example, patient E14,

381 who was already introduced in **Fig. 3f** as a representative example of low inter-metastatic

382 heterogeneity, showed a strong association between deep-invading area PT5 and a metastatic

383 lineage that was present across multiple host sites (peritoneum, liver, locoregional lymph nodes

384 and tumor deposits). Examining this patient's H&E images, we observed that PT5 was the only

385 sampled primary tumor region that directly abutted and invaded into the pericolonic fat

386 (**Supplementary Fig. 8**). It is therefore plausible that this region would be the ancestor of all seven

387 synchronous peritoneal metastases in this patient.

388

389 Almost identical patterns were observed in several other cases. In patient E18, primary tumor areas

390 PT6 and PT7 – the deepest-invading of all 11 sampled regions – were genetically clearly distinct

391 from the rest of the primary tumor and perfectly matched a large metastatic clade which comprised
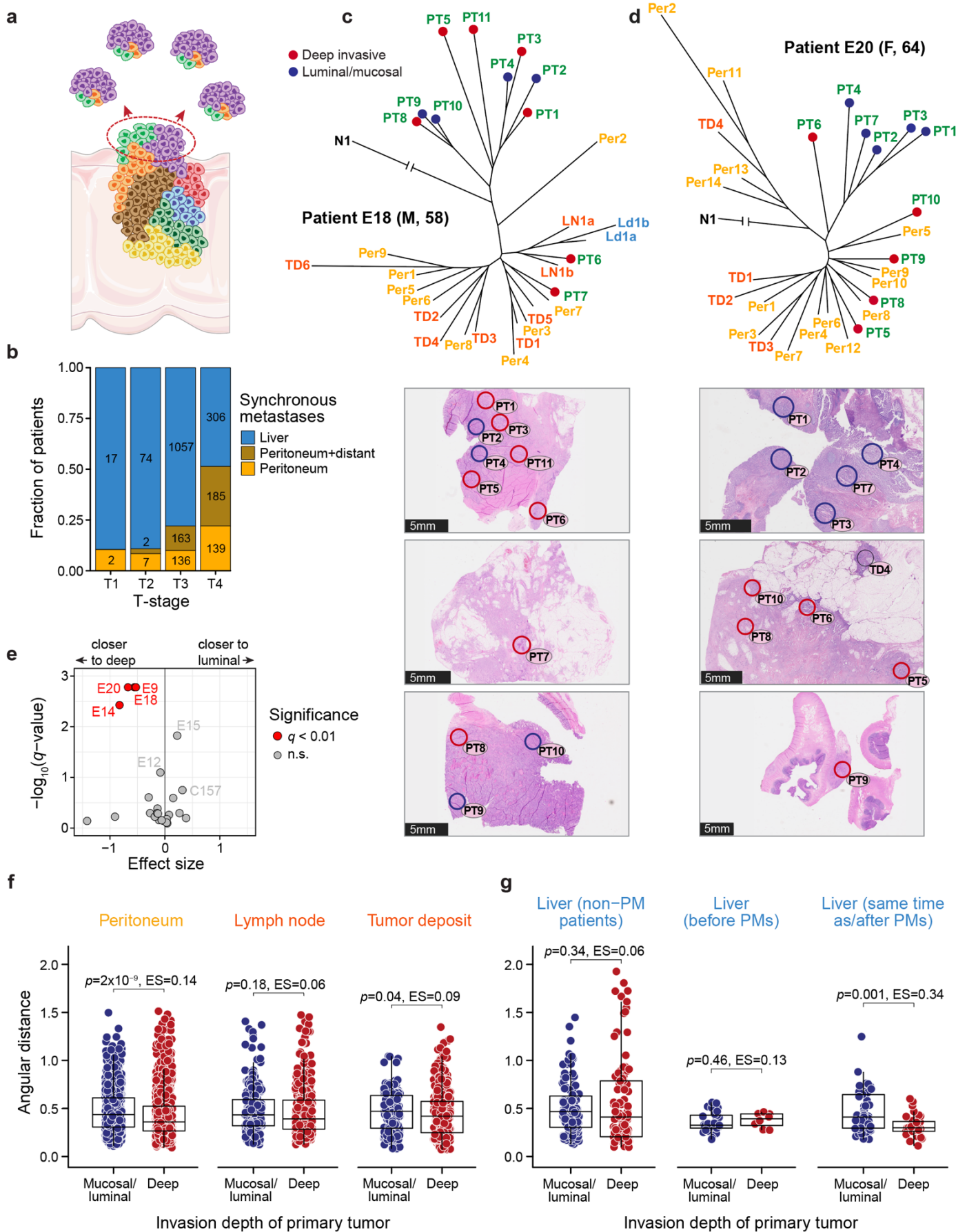
Figure 4. Peritoneal metastases associate with deep-invading primary tumor regions. a, Schematic of a T4 stage primary tumor breaching the peritoneal lining (red highlighted region) and seeding peritoneal metastases that are enriched for lineages that are in the breach area **b,** Metastasis types observed in stage IV patients stratified by T-stage. Bars are labeled with the number of patients in each category. Data adapted from Lemmens et al.[30]. **c-d,** Phylogenetic trees for patients E18 **(c)** and E20 **(d)** along with histological images showing the precise anatomical location of primary tumor samples. *Red circles*, deep-invading regions. *Blue circles*, luminal/mucosal regions. **e,** Association of peritoneal metastases (as a group) with deep-invading vs. luminal primary tumor for each patient. For each peritoneal metastasis, we calculate the ratio of its angular distances to the closest deep-invading and closest luminal/mucosal region (lesion-depth ratio). This value is then averaged across all lesions to quantify their overall proximity to deep-invading vs. luminal regions. x-axis: $\log_2$-ratio of the *observed* average lesion-depth ratio to the *expected* average lesion-depth ratio (median of 10,000 permutations of primary tumor regions' invasion-depth labels within each patient). y-axis: $-\log_{10}$ p-values from two-sided permutation tests for each patient, with correction for multiple hypothesis testing (q-values). Patients with significant peritoneal metastasis similarity to either deep-invading or luminal/mucosal regions are highlighted in red. **f,** Pairwise angular distances between metastases and deep-invading vs. luminal/mucosal primary tumor regions. Each point is the angular distance between a metastasis and a primary tumor region of the indicated invasion depth. All unique combinations of metastases and primary tumor regions within the same patient are included. p-values and effect sizes from two-sided Wilcoxon rank sum tests. **g,** Pairwise angular distances between liver metastases and deep-invading vs. luminal/mucosal primary tumor regions, separated by liver metastasis timing with respect to the earliest diagnosed peritoneal metastasis (PM). *Left*, patients with no peritoneal metastases, only liver metastases. *Center,* liver metastases diagnosed at least 3 months before peritoneal metastases. *Right*, liver metastases diagnosed at the same time or after peritoneal metastases.

392　　8 anatomically distinct peritoneal metastases, 7 locoregional metastases as well as a distant lymph

393　　node metastasis (**Fig. 4c**). In Patient E20, four deep-invading regions (three of them sampled from

394　　a front of primary tumor that was abutting and pushing into the pericolonic fat) clustered with 10

395　　peritoneal metastases and three tumor deposits, while all five luminal samples formed an unrelated

396　　branch elsewhere on the phylogenetic tree (**Fig. 4d**).

397

398　　To quantify the association between the deep-invading edge and clusters of peritoneal metastases

399　　more formally, we conducted a permutation-based statistical test which evaluated whether

400　　peritoneal metastases *as a group* were more closely related to the deep-invading or luminal

401　　primary tumor in each patient (**Fig. 4e**, with details in legend). This analysis confirmed a

402　　significant (q<0.01) clustering of peritoneal metastases with the deep-invading tumor edge in

403　　multiple patients, while no such clustering was observed for luminal primary tumor regions.

404　　Similarly, we found no significant association between the deep invading edge and groups of

405　　lymph node or liver metastases; one patient's (E20) tumor deposits scored in the significant range

406　　(**Supplementary Fig. 9**).

407

408　　Since the analysis above rewards scenarios in which *multiple* lesions of a given type (peritoneal,

409　　locoregional, liver) are non-randomly associated with either the deep-invading or luminal edge,

410　　we wanted to provide an additional quantification that directly assesses the proximity of *individual*

411　　metastatic lesions to different parts of the primary tumor. We therefore evaluated all pairwise

412　　angular distances from metastatic lesions to their matching deep-invading and luminal primary

413　　tumor regions. We found that also in this global view, peritoneal metastases had significantly

414　　shorter distances to deep-invading primary tumor samples (**Fig. 4f**). Lymph node metastases, on

415　　the other hand, were equally closely related to deep-invading and luminal areas, suggesting that

416　　these lesions do not preferentially originate at the invasive front. Tumor deposits showed an

417　　intermediate association with the deep edge. Liver metastases exhibited a noteworthy pattern. They

418　　were not preferentially associated with the luminal or deep-invading edge in patients who had no

419　　peritoneal metastases, or in patients in whom peritoneal metastases occurred after the liver lesions

420　　had already been resected. However, we did see an association between liver metastases and the

421　　deep-invading edge in patients who had prior or synchronous peritoneal metastases (**Fig. 4g**). This

422　　observation raised the question whether liver metastases in these patients might have been seeded

23

423   by peritoneal metastases – a plausible hypothesis given that the visceral peritoneum (which makes

424   up 70% of the peritoneal surface), drains into the portal vein. Disseminating cancer cells that

425   originated at the deep-invading edge of the primary tumor and colonized the visceral peritoneum

426   would thus encounter the liver as their first capillary bed. We therefore turned to a closer

427   examination of the lineage relationship between peritoneal and distant metastases.

428

429   ***Most peritoneal metastases do not share a common evolutionary origin with distant metastases***

430   Do peritoneal lesions have distinct subclonal origins from 'true' distant metastases in more remote

431   organs like the liver or the lungs, or are all stage IV-defining metastatic lesions clonally related?

432   Examining patient phylogenies, we found several cases in which peritoneal and distant metastases

433   clearly did share a common subclonal origin. For example, peritoneal metastases were closely

434   related to distant metastases in patient E7 who received surgery for a primary tumor in the caecum

435   and synchronous metastases to both ovaries. The patient was disease-free until she relapsed almost

436   4 years later with metastases to the peritoneum and the lungs (detailed clinical timeline in

437   **Supplementary Fig. 3**). The phylogeny showed a clear separation between the primary tumor and

438   all metastases (**Fig. 5a**) and, in conjunction with the patient's clinical history, suggested that the

439   ovarian lesions could have been involved in seeding peritoneal metastases. This scenario seems

440   particularly plausible because the primary tumor was T3 stage and thus had not visibly penetrated

441   the peritoneal lining yet. In contrast, most of patient E5's synchronous peritoneal metastases

442   appeared clonally unrelated to their synchronous ovarian and metachronous liver metastases (**Fig.**

443   **5b**). The liver metastases consisted of three anatomically distinct lesions (Liv1-3) that were

444   resected less than one year after the primary tumor. Although they were recovered from different

445   liver segments, they clustered in a tight monophyletic clade, as we often observe for liver

446   metastases (**Fig. 2e**). The ovarian metastasis was much more clonally diverse, with its different

447   multi-region samples (OvH1a-d) mapping to different branches of the phylogenetic tree. Two

448   peritoneal metastases (Per3-4) appeared clonally related to parts of the ovarian metastasis and

449   deep-invading primary tumor region PT10, but most peritoneal lesions located to distinct clades

450   that had no special relationship to any of the distant-metastatic samples.

451

452   To identify larger trends in the relationship between peritoneal and distant metastases across the

453   whole cohort, we recorded the genetic distance of each peritoneal metastasis to its closest distant
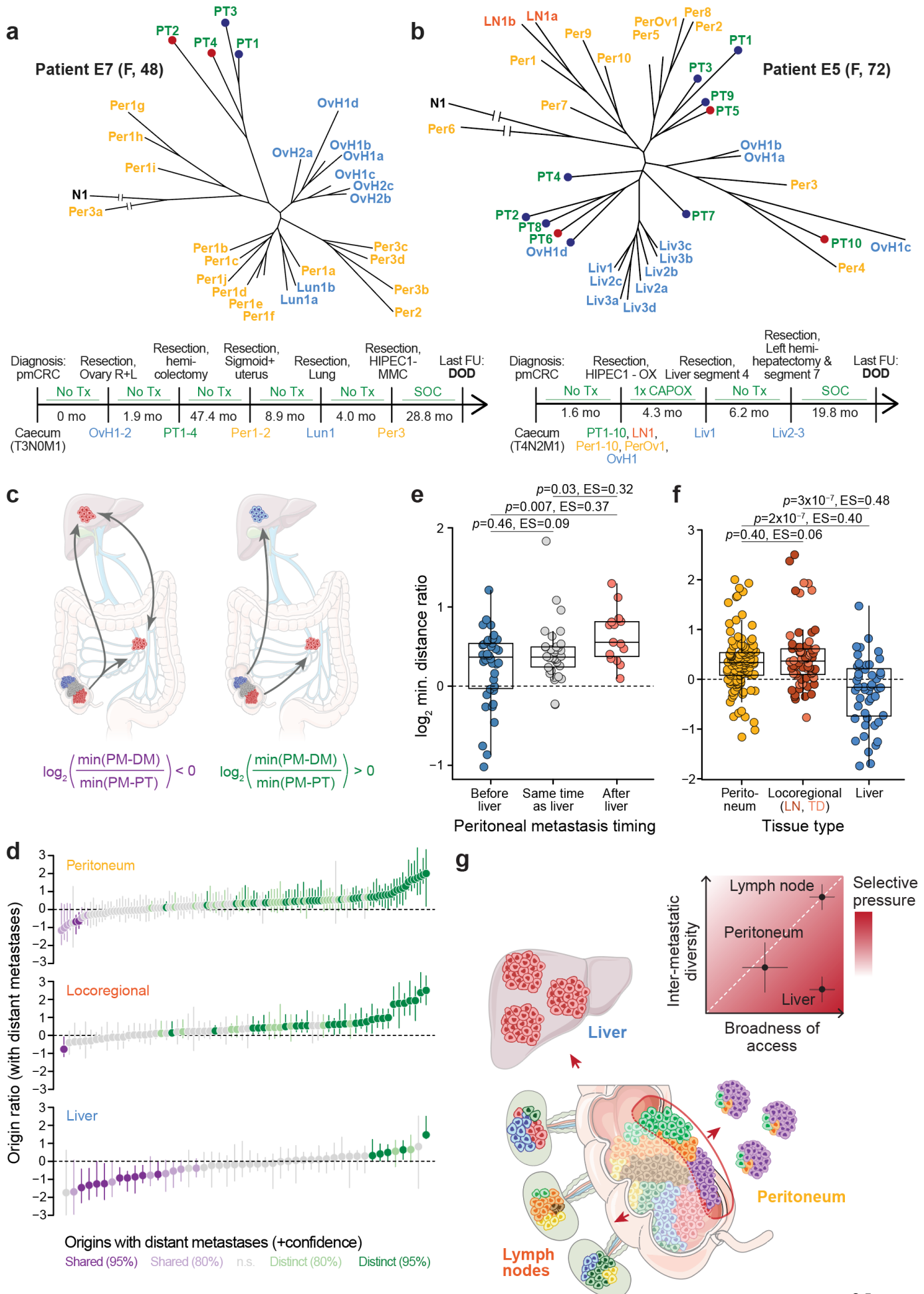
Figure 5. Peritoneal and distant metastases typically have distinct evolutionary origins. a, Phylogenetic tree and clinical timeline for patient E7. OvH, Ovarian metastasis of suspected hematogenous origin by pathological examination (tumor growth within the parenchyma but not on the ovarian surface). **b,** Phylogenetic tree and clinical timeline for patient E5. **c,** Schematic depicting two possibilities for the lineage relationship between peritoneal (PM) and distant metastases (DM). *Left*, peritoneal and distant metastases have a common subclonal origin. This could mean that they are both seeded from the same primary tumor lineage, or that they gave rise to each other. In this case, the origin ratio, defined as $\log2(\frac{\min{(PM-DM)}}{\min{(PM-PT)}})$, is expected to be smaller than 0. *Right*, peritoneal and distant metastases have distinct origins in the primary tumor. In this case, the origin ratio is expected to be larger than 0. **d,** Origin ratios for each peritoneal, locoregional, and liver metastases. Specifically, the origin ratio for peritoneal metastases is as described above, for locoregional metastases it is $\log2(\frac{\min{(LN-DM)}}{\min{(LN-PT)}})$ and for liver metastases it is $\log2(\frac{\min{(Liv-DM)}}{\min{(Liv-PT)}})$. Bootstrapped 95% confidence intervals based on 1,000 iterations of randomly resampled polyguanine markers. Confidence values for origin classifications are based on the upper bound of 80% or 95% confidence intervals. **e,** Peritoneal-liver metastasis origin ratios $(\log2(\frac{\min{(PM-Liv)}}{\min{(PM-PT)}}))$ for peritoneal metastases arising before, synchronously with, or after liver metastases. *Left*, peritoneal metastases arising at least 3 months prior to the earliest detected liver metastasis; *center*, within 3 months of the earliest liver metastasis; *right*, at least 3 months after the earliest liver metastasis. **f,** Direct comparison of origin ratios for peritoneal, locoregional and liver lesions metastases (same data as in (d)). Locoregional point color differentiates lymph node metastases and tumor deposits. *P*-values and effect sizes based on independent pairwise comparisons using two-sided Wilcoxon rank sum tests. **g,** Summary schematic. Genetic diversity from the primary tumor (colored cells) is transferred most efficiently to locoregional metastases, less efficiently to peritoneal metastases, and least efficiently to liver metastases, resulting in decreasing inter-metastatic diversity across these host sites (inset). The broadness of tumor cell access to the relevant migration routes is high for cells undergoing lymphatic or hematogenous metastasis, and more restricted for cells undergoing peritoneal metastasis. By jointly evaluating broadness of access and inter-metastatic diversity, we deduce that selective pressures are highest during liver metastasis (see discussion for details).

454   metastasis ($min(PM - DM)$), as well as its closest primary tumor sample ($min(PM - PT)$, **Fig.**

455   **5c**). The log$_2$ ratio of these two values (hereafter "origin ratio" for simplicity) is negative whenever

456   a peritoneal metastasis associates closely with a distant metastasis while being further removed

457   from the primary tumor. This can either indicate that both the peritoneal and the distant metastasis

458   arose from related lineages in the primary tumor, or that they seeded each other. Conversely, the

459   ratio is positive if the peritoneal metastasis is more closely related to the primary tumor than to

460   any distant metastasis, indicating that the two lesions likely arose from distinct primary tumor

461   subclones.

462

463   Examining origin ratios across *n*=129 peritoneal lesions that arose in patients who also had distant

464   metastases, we noticed a clear skewing towards positive values, meaning that most peritoneal

465   metastases were more closely related to the primary tumor than to a distant metastasis (**Fig. 5d**).

466   These results were reminiscent of a prior study in which we had investigated the lineage

467   relationships between lymph node and distant metastases and found that in most (65%) colorectal

468   cancer patients, lymph node metastases did not share a subclonal origin with distant metastases

469   but originated directly in the primary tumor[13]. Other studies subsequently reached the same

470   conclusions[31]. Notably, we found that the small subset of peritoneal lesions that were more closely

471   related to a distant metastasis than to the primary tumor (purple bars in the top panel of **Fig. 5d**)

472   was enriched for patients who were diagnosed with liver metastases at the same time or after their

473   peritoneal metastasis resection (**Fig. 5e**). That was the same patient group that had exhibited

474   uncharacteristically close associations between the deep-invading edge and liver metastases in **Fig.**

475   **4g**, providing further support for the idea that peritoneal-to-liver seeding is relatively common

476   when peritoneal metastases precede or coincide with liver metastases.

477

478   Calculating origin ratios for locoregional metastases (lymph nodes and tumor deposits) in the

479   peritoneal metastasis cohort, we found a distribution that resembled our previous findings (76% of

480   locoregional metastases associated more closely with the primary tumor while 24% resembled

481   distant metastases more closely). In a direct comparison, we found no difference between the origin

482   ratio distributions of locoregional and peritoneal metastases (**Fig. 5f**), suggesting that both

483   metastasis types had the same close relationship to the primary tumor and the same comparatively

484   weak link to distant metastases. Importantly, when we calculated origin ratios for liver metastases,

485   we observed a much more pronounced skewing towards negative values (**Fig. 5d**), indicating that

486   liver metastases typically arose from the same subclonal lineage as other distant metastases[14]. The

487   difference between the origin ratios of peritoneal/lymph node metastases and liver metastases was

488   highly significant (**Fig. 5f**). A multiple linear regression which included the ratio between the

489   number of sampled primary tumor areas and number of distant metastases (a potential confounder)

490   as an additional independent variable also recovered highly significant differences between origin

491   ratios for liver metastases on the one hand and peritoneal and locoregional metastases on the other

492   hand (peritoneum vs. liver $p=1.4 \times 10^{-5}$; locoregional vs. liver $p=3 \times 10^{-6}$; ratio between the number

493   of sampled primary tumor areas and number of distant metastases $p=0.55$). We conclude that just

494   like locoregional metastases, peritoneal metastases typically originate in the primary tumor and

495   mostly do not share a common evolutionary origin with distant metastases.

496

497   **Discussion**

498

499   In this study, we have traced the origins of hundreds of colorectal cancer peritoneal metastases,

500   locating them on a detailed genetic map with the primary tumor and other locoregional and distant

501   metastases as landmarks for comparison. Our exhaustive sampling scheme allowed us to make

502   several novel observations. First, we were able to assess metastatic randomness in peritoneal

503   metastases in direct comparison with locoregional and liver metastases. We observed that

504   peritoneal metastases showed intermediate levels of inter-metastatic heterogeneity: they were less

505   diverse than locoregional metastases but more diverse than liver metastases. Second, we found

506   that peritoneal – but not lymph node or liver – metastases tended to associate with lineages (or

507   subclones) that were located on the deep-invading edge of the primary tumor. This result is

508   consistent with decades of clinical experience showing that patients whose primary tumor has

509   breached the serosal lining face a much-increased risk of peritoneal metastasis. Finally, we found

510   that peritoneal metastases typically have distinct evolutionary origins from metastases in distant

511   organs like the liver or lungs. This surprising discovery can perhaps be explained by their

512   preferential seeding from the deep-invading front, a predilection that is not shown by other types

513   of metastases. Patients who develop liver metastases following peritoneal metastases appear to be

514   an exception: we often observe a shared subclonal origin of metastatic lesions in these cases, and

515   we suspect that cancer cells may reach the liver from the peritoneum in these cases.

516

517   What can these observations in their totality teach us about the cells that seed peritoneal metastases

518   in humans? Is a specialized trait required for peritoneal metastasis formation? The data suggest

519   that the peritoneal-metastatic process exerts *less* stringent selective pressures on disseminating

520   tumor cells than the liver-metastatic process, resulting in a greater variety of subclones that can

521   successfully complete it. Hence, there is a relative lack of requirement for specialized traits, at

522   least in comparison with the liver. Specifically, the following line of argument can be considered:

523   The degree of metastatic diversity in a host organ is determined by i) the broadness of tumor cell

524   access to that organ and by ii) the strength of selective pressures encountered by tumor cells during

525   dissemination and colonization. If access is broad and plentiful, and selective pressures are low,

526   many subclones will successfully complete the process and metastases will exhibit high inter- and

527   intra-lesion diversity. Lymph node metastasis appears to be a paradigm for this type of metastasis.

528   Lymphatic vessels are typically broadly distributed in and around colorectal cancers[32], giving most

529   lineages access to this migration route (although lymphatic transport can sometimes be hampered

530   by the physical forces generated during tumor growth[33]). In line with this observation, lymph node

531   metastases are equally likely to originate in luminal or deep tumor areas in our data. Once cells

532   enter the lymphatics, shear and oxidative stresses are low and beneficial lipids that protect cells

533   from ferroptosis abound[16]. The broadness of access to lymphatics in combination with low

534   selective pressures in the environment result in high levels of genetic diversity in and among lymph

535   node metastases. Tumor cells require few specialized traits to succeed.

536

537   Liver metastasis seems to present a much greater challenge. Access to the relevant migration route

538   – the blood vessel – is likely to be just as broad as for the lymphatics, as all viable tumor areas

539   must have at least a minimal vascular supply. Liver metastases in patients who do not (yet) have

540   peritoneal metastases do not preferentially associate with luminal or deep areas. However, since

541   liver metastases show striking levels of genetic homogeneity, both within and among lesions, we

542   must conclude that the migration and/or colonization process exerts strong selective pressures onto

543   cancer cells, resulting in a severe "thinning" of lineages that can survive the process. Again, this

544   is consistent with many functional studies that have shown the systemic circulation to be a highly

545   challenging environment for cancer cells[17]. Liver metastases probably arise from select lineages

546   that have acquired a trait that confers a selective advantage in this context.

547

548   Extending the same logic to the peritoneum, we can cautiously conclude a few points: First, access

549   to the peritoneal cavity is likely to be more restricted than access to the lymphatics or the blood.

550   Only subclones that have completely breached the colon wall can easily reach the peritoneum and

551   seed metastases – for all other subclones, the journey is far and the seeding rate probably

552   negligible. This unique spatial restriction should dramatically restrict the diversity of peritoneal

553   metastases. However, metastatic diversity in the peritoneum trumps the liver, although access to

554   the organ is much less broad. We believe that this can only be explained by relatively lax selective

555   pressures: many of the cells that do have access to the peritoneal cavity will be able to grow there,

556   resulting in higher diversity despite restricted access (summary cartoon in **Fig. 5g**). It is possible

557   that cancer cells benefit from being able to reach the peritoneum without having to expose

558   themselves to the systemic circulation – a particularly harsh environment as discussed above.

559

560   If cells that form peritoneal metastases indeed have not yet evolved to withstand the severe

561   selective pressures that are exerted upon them during systemic dissemination, we may perhaps

562   look hopefully toward future treatment options for patients with this disease. One possible reason

563   that even a single resectable liver metastasis portends a poorer prognosis than many (equally

564   resectable) lymph node metastases might be that the occurrence of the liver metastasis signals the

565   presence of a very dangerous lineage. This species can travel in the blood stream and grow even

566   in unfriendly environments, darkening the outlook for the patient. If peritoneal-metastatic cells –

567   much like locoregional metastases – indeed represent a less evolved precursor of this lethal cell

568   type, long-term disease control could perhaps still be achieved if we had more effective local

569   management tools. For example, if more complete resections could be achieved through advanced

570   intra-operative imaging, outcomes might improve further. Finally, the distinct genetic properties

571   of peritoneal metastases, which in some respects recapitulate features of locoregional metastases,

572   raise the question whether peritoneal metastases should be staged separately from metastases in

573   other distant organs.

574   **Methods**

575

576   **Tissue samples**

577   *Peritoneal metastasis patient cohort*

578   Tumor specimens from two institutions (The St. Antonius Hospital, Nieuwegein, the Netherlands

579   and Massachusetts General Hospital, Boston, USA) were included in this study after approval from

580   each hospital's institutional review board (MGH IRB and Medical Research Ethics Committees

581   United in Nieuwegein), and in accordance with the Declaration of Helsinki. Since polyguanine

582   fingerprinting is a very limited interrogation of non-coding genomic regions, it is performed under

583   a waiver of consent. We searched internal databases for patients who had undergone resection of

584   at least one peritoneal metastasis from colorectal cancer. Search results were then subset for cases

585   with an available primary tumor. We reviewed hematoxylin & eosin (H&E)-stained tissue sections

586   for candidate patients to identify those that had tumors of sufficient size and purity. For example,

587   cases were excluded from consideration if they had very small peritoneal metastases consisting of

588   only a small number of scattered tumor cells, or if primary tumors exhibited extensive necrosis

589   and treatment effects. In this manner, we identified 20 suitable patients from St. Antonius (E1-

590   E20) and 4 patients from Massachusetts General Hospital (C146, C154, C157, C158). In all these

591   cases, both primary tumor and metastases consisted of high-quality tumor tissue. This cohort of 24

592   patients was supplemented with two patients (C38 and C89) with colorectal cancer and peritoneal

593   metastases from previously published studies[13,14].

594

595   *Additional tumor samples*

596   To compare the genetic properties of peritoneal metastases to distant lesions in other organs, we

597   included in various analyses throughout the paper polyguanine fingerprints from n=25 additional

598   patients with metastatic colorectal cancer to the liver from previously published studies[13,14]. As in

599   Reiter et al.[14], we also included 5 patients with colorectal cancer and liver metastases whose

600   phylogenies were generated from whole-exome sequencing data (patients CRC1-5)[34]. These 30

601   retrospective patients contributed only to analyses involving liver metastases. The 5 whole-exome

602   phylogenies CRC1-5 were only included in analyses involving root diversity scores (RDS), which

603   can be calculated independently of the underlying data type if a phylogenetic tree is available.

604   Finally, 3 previously unpublished patients with metastatic colorectal cancer are described in this

605 study which are not part of the peritoneal metastasis cohort. These patients (C159, C161, C186)
606 either had no peritoneal metastases (C186), or only had peritoneal metastasis samples recovered
607 at autopsy (C159 and C186), a biologically distinct scenario which we did not want to mix with
608 the main cohort which consisted exclusively of surgical resection specimens. These patients were
609 only used to compare polyguanine vs. low-pass whole genome sequencing-derived phylogenies in
610 **Fig. 1c-e** and **Supplementary Fig. 2**; their data are not included in any other analyses.

611

612 *Metastasis characteristics and naming conventions*
613 Anatomically distinct metastases were given distinct numbers, in line with our previously used
614 naming convention[13,14]. For example, Per1 and Per2 represent two spatially separated peritoneal
615 lesions. Multiple samples from the same metastatic lesion are additionally labeled with letters, e.g.
616 Per1a and Per1b. Metastases were classified as synchronous if they were present at the time of
617 primary tumor resection, and metachronous if they were resected more than 3 months after that.
618 This study distinguishes between lymph node metastases (locoregional metastases that retain
619 clearly identifiable lymphoid tissue) and tumor deposits (locoregional metastases that show no
620 evidence of lymphoid tissue). These categories are thought to be potentially biologically distinct[35].
621 For patients C38 and C89 who were included from previous studies, histological images were no
622 longer available, and we could not make this distinction. Therefore, in analyses that distinguish
623 between lymph node metastases and tumor deposits (as opposed to treating them as one category),
624 locoregional metastases from C38 and C89 were excluded. In analyses of treatment effects, we
625 generally considered systemic chemotherapy separately from hyperthermic intraperitoneal
626 chemotherapy (HIPEC), as the latter is a local intervention. We refer to distant metastases in the
627 liver, lungs, ovaries or distant lymph nodes as "untreated" if they were never exposed to systemic
628 chemotherapy. Peritoneal metastases, however, were only considered untreated if they had
629 experienced neither chemotherapy nor HIPEC. Patient E13's liver metastasis (Liv1) arose after
630 treatment with HIPEC only, we therefore retain it in the untreated category.

631

632 *Histology and tissue processing*
633 A board-certified gastrointestinal pathologist (J.K.L) reviewed H&E slides or images and carefully
634 annotated tumor regions. Bulky tumor was sampled with 1.5-2 mm core biopsies. For smaller
635 regions of interest, 8 μm tissue sections were macrodissected under the microscope. Tissues were

636   deparaffinized with xylene and digested with proteinase K overnight. DNA was extracted with

637   phenol-chloroform and precipitated with ethanol and sodium acetate, as previously described[13,14].

638

639   **Polyguanine fingerprinting**

640   Detailed descriptions of the primer sequences and PCR protocol for amplification of polyguanine

641   repeats have been previously published[13,14]. We genotyped between 18 and 45 markers per patient

642   (mean = 31.3 markers/patient). Genotypes for each marker and tumor sample were acquired in

643   triplicate for a total of 73,859 individual PCRs that contributed to the data set. Peak information

644   for each sample, polyguanine marker, and replicate was extracted from GeneMapper 4.0 and used

645   as input to a previously described automated analysis pipeline[13]. We will briefly explain the main

646   analysis steps here, but a more detailed description can be found in the original publication. In a

647   first pre-processing step, we removed all reactions that did not show robust amplification, i.e.

648   where fragment fluorescence intensity was less than 10% of the average intensity for that

649   polyguanine marker and patient. After intensity filtering, we proceeded to examine the three PCR

650   replicates for each marker and sample and chose the best ("representative") replicate for further

651   analysis, as described in detail in Naxerova et al.[13]. Briefly, for each sample, we calculated the

652   Jensen-Shannon distance (JSD, the square root of the Jensen-Shannon divergence[36]) among all

653   replicate pairs. Two replicates were classified as identical if their JSD was less than 0.11. Among

654   the pairs of replicates that were classified as identical, we chose the pair with the lowest JSD and

655   selected the replicate with the higher intensity to be the representative replicate for the sample. If

656   no two replicates were classified as identical, either the sample was excluded, or the marker was

657   excluded across all samples of a given subject. Because our phylogenetic reconstruction method

658   is intolerant to missing data, we removed polyguanine markers from a patient's data set if they

659   failed to amplify for too many samples, or we removed tumor samples if they had too many missing

660   genotypes (e.g. due to suboptimal DNA quality). Balancing the dual goals of retaining as many

661   markers and as many tumor samples as possible for each patient, we chose to remove between 1-

662   15% of polyguanine marker genotypes per patient to obtain a valid genotype across all samples.

663   We ran this entire pipeline once at the beginning of the analysis stage for all samples and then

664   executed an impurity exclusion step to remove samples that did not meet minimum purity

665   standards. Due to the introduction of the purity-robust angular distance method, we were able to

666   slightly relax the stringency of impurity exclusion in comparison with previous studies[13,14]. The

667 adjusted impurity exclusion approach was identical to the published version[13], except that for each

668 sample, we now fitted a linear regression, with the 'calibrator distances to normal reference' as

669 response and 'sample distances to normal reference' as explanatory variables. If the slope was

670 smaller than 0.35, the sample was excluded from the analysis. After impurity exclusion, the entire

671 pipeline was re-run on the remaining set of sufficiently pure samples to generate the final data set

672 on which all subsequent analyses were based. This data set is freely available at

673 https://github.com/agorelick/peritoneal_metastasis. The automated pipeline is implemented as an

674 installable R library and can be downloaded at https://github.com/agorelick/polyG.

675

Phylogenetic reconstruction and analysis of evolutionary trees

676

Phylogenetic reconstruction from polyguanine fingerprints

677

678 For each patient, we constructed a distance matrix containing pairwise, purity-robust angular

679 distances between samples. More details on this distance measure are provided in the

680 accompanying **Supplementary Note**. In brief, the stutter distribution derived from each

681 polyguanine locus in each sample was simplified to its mean fragment length[15]. Each tumor sample

682 is thus represented by a vector of length n, with n being the number of measured polyguanine

683 markers. We subtracted from this vector the mean lengths measured in the normal tissue control,

684 thus creating the "polyguanine fingerprint" which encodes the sample's somatic mutations across

685 all polyguanine loci. Next, all polyguanine fingerprints were normalized to unit length. The

686 angular distance between two unit length polyguanine fingerprints x and y is then defined as

687 $\arccos (x \cdot y)$. Phylogenies were then constructed from the angular distance matrices using the

688 neighbor-joining method (implemented in the *ape* R package[37]). The normal germline sample was

689 attached post-hoc to each patient's phylogeny by connecting it to the last internal node created by

690 the neighbor-joining algorithm. Please note that the branch *length* leading to the normal tissue

691 control sample has no meaning in this context (to highlight this, we introduce a break in the branch

692 leading to the normal tissue samples in all phylogenies). Phylogenies were annotated with

693 confidence values based on 1,000 bootstrap replicates constructed by randomly re-sampling

694 polyguanine markers with replacement.

695

Pre-processing for inter-lesion heterogeneity analyses

696

34

697   In some cases, we sampled individual metastatic lesions multiple times. These samples were useful
698   to assess intra-metastatic heterogeneity. However, for all analyses of inter-metastatic diversity
699   (described below), we had to choose *one* sample to represent the metastasis and thus make it
700   comparable to other metastases that were only sampled once. Therefore, for all analyses involving
701   pairwise inter-lesion angular distances or root diversity scores, we generated a "collapsed" version
702   of each patient's phylogenetic tree. In the collapsed tree, each distinct metastatic lesion is
703   represented by only one sample. For simplicity, we chose the sample that received the letter "a" in
704   the initial sample processing workflow, resulting in a random choice from a biological point of
705   view.

706

707   *Metastasis-specific root diversity score (RDS)*

708   To assess the phylogenetic diversity of multiple, anatomically distinct metastases with respect to
709   the multi-region sampled primary tumor, we calculated the root diversity score (RDS), defined as
710   the probability that at least l out of m metastases form a monophyletic clade in a tree with $n = k + m$
711   tumor samples[14]. The RDS reflects the probability that a tree with an equal or more extreme
712   clustering of metastases occurs by chance alone. In this study, we calculated "metastasis-specific"
713   RDS values by constructing collapsed phylogenetic trees that only contain primary tumor samples
714   and samples from a metastasis group of interest (peritoneal, lymph node, tumor deposit, liver).
715   This approach avoids that clustering of different metastasis subtypes (e.g. clustering of both lymph
716   node and liver metastases away from the primary tumor) inflates RDSs. Metastasis-specific RDS
717   values thus quantify the degree of separation *between the primary tumor and a specific metastasis*
718   *type of interest* (unencumbered by the position *other* metastases on the phylogenetic tree). R code
719   that can be used to calculate RDS values for any phylogenetic tree has been packaged into an
720   installable R library available at https://github.com/agorelick/rds.

721

Analysis of somatic copy number alterations (SCNAs)

723   *Low-pass whole genome sequencing*

724   Low-pass whole genome sequencing (lpWGS, ~1x) libraries were prepared from genomic DNA
725   using the NEBNext Ultra DNA Library Prep Kit for Illumina. Quality of raw sequencing output
726   was verified using FASTQC[38] (v0.12.1) and sequencing reads were aligned to the human reference

35

727 genome (version humanG1Kv37) with the BWA-MEM algorithm[39] (v0.7.15) with soft-clipping

728 enabled.

729

730 *SCNA-based trees from lpWGS data*

731 lpWGS-based genomic copy number profiles were generated using the QDNASeq[40] and ACE[41] R

732 packages to obtain copy number estimates in 1Mb genomic bins. For each patient, the QDNAseq

733 R package was used to generate read counts in 1Mb bins for each BAM file, based on reference

734 human genome hs37d5. To correct read counts for bins' variable GC content and mappability, we

735 estimated correction factors using *estimateCorrection* function with default parameters after first

736 excluding sex chromosomes, as well as blacklisted and low mappability (< 25) regions. To retain

737 sex chromosomes in the corrected read counts (X and Y are excluded in this output by default by

738 QDNAseq), as per the authors' instructions, the filter on sex chromosomes was then removed and

739 the corrections were applied to bins from all chromosomes. The corrected read counts were then

740 normalized, outliers were smoothed, bin counts were segmented, and copy number segments were

741 normalized, following instructions in the QDNAseq documentation with default parameters. For

742 each sample, the ACE package was then used to obtain purity and ploidy-corrected total copy

743 number.

744

745 Briefly, given an overall average ploidy value (usually 2 or 4), ACE exploits the notion that clonal

746 copy number alterations create segments with integer-valued total copy number to find purity

747 values that maximize the number of segments with integer values (indicating that the tumor purity

748 and ploidy have correctly been adjusted for). For a given patient, we manually reviewed and fine-

749 tuned the purity/ploidy fits from ACE for each sample to best-align the likely-clonal segments,

750 such that they had the same integer copy number values in each sample (while also preserving

751 their overall similarity across all tumor samples). The 1Mb copy number bins were then corrected

752 for these purity/ploidy values, and the resulting total copy number profiles were used to calculate

753 Euclidean distances between each pair of samples. Finally, the neighbor-joining algorithm was

754 used to construct phylogenetic trees for each patient's copy number data. Confidence values for

755 copy number-based phylogenetic trees were generated based on 1,000 bootstrap replicates

756 constructed by randomly sampling entire chromosomes with replacement from the 1Mb bin data.

757

758 *Tests for concordance between polyguanine and lpWGS-based phylogenetic data*

759 The similarity between two phylogenetic trees representing the same set of samples was quantified

760 using the quartet similarity (implemented in the *Quartet* R library, which employs the tqDist

761 software[42]). Given two unrooted, bifurcating trees of size *n* with the same set of samples, the

762 quartet similarity is defined as the fraction of all possible 4-sample subtrees that are common

763 between them. To test whether two phylogenetic trees were more similar than expected by chance,

764 we used a permutation-based approach, comparing the true quartet similarity between two trees to

765 a null distribution generated by randomly permuting the tip labels on one of the two trees 10,000

766 times. A one-sided *p*-value was calculated as the fraction of random permutations with a quartet

767 similarity at least as great as the similarity observed, with a pseudocount of 1 added to both the

768 numerator and denominator. A similar permutation-based approach was used to test the similarity

769 between two distance matrices for the same set of samples. Here, the rows and columns of the

770 matrices were both ordered identically, and Spearman's correlation coefficient was calculated

771 between the values in each matrix's upper triangle (excluding the diagonal). To compare this to a

772 null distribution, we randomly permuted the row and column labels in one of the matrices 10,000

773 times, each time reordering its rows and columns to match the non-permuted matrix and

774 calculating a new Spearman correlation. A one-sided *p*-value for the significance of the matrices'

775 similarity was calculated as described above.

776

777 **Clonal evolution inference for patient C157**

778 *Whole exome sequencing data processing*

779 Whole exome sequencing libraries were prepared from genomic DNA using the Human Core

780 Exome kit by Twist Bioscience and sequenced to an average depth of 184x. Quality of raw

781 sequencing output was verified using FASTQC[38], and adapter sequences were trimmed using

782 Cutadapt[43] (v4.1). Sequencing reads were pre-processed following the GATK Best Practices

783 workflow[44] for variant discovery. Briefly, sequencing reads were aligned to the human reference

784 genome (version humanG1Kv37) with the BWA-MEM algorithm (v0.7.15). Duplicate reads were

785 removed using GATK (v4.1.9.0) *MarkDuplicatesSpark*. Base scores were recalibrated using

786 GATK *BaseRecalibrator* and *ApplyBQSR* using all polymorphic sites from dbSNP (build 151) as

787 the list of known sites for exclusion. After pre-processing sequencing data, somatic mutations were

788 called using *Mutect2* in multi-sample mode using a matched normal sample, a panel of normal

37

789   provided by GATK, and germline allele frequencies provided by gnomAD[45] using default
790   arguments. To reduce potential false positives due to formalin fixation, orientation bias artifact
791   priors were learned using *LearnReadOrientationModel* and the resulting variants were then filtered
792   using *FilterMutectCalls*. MAF files were created from VCF using vcf2maf (v1.6.21). Mutations
793   were annotated for known/predicted oncogenic effects using OncoKB[46] (v3.3, accessed Dec 5,
794   2023) and considered potentially oncogenic if they were annotated by OncoKB as "Oncogenic" or
795   "Likely Oncogenic", or if the variant was classified as "Loss-of-function" or "Likely Loss-of-
796   function". The FACETS software[47] (v0.6.2) was used to estimate purity and ploidy and generate
797   allele-specific copy number profiles for each sample. Mutations were then annotated with
798   estimated cancer cell fractions (CCFs) as previously described[48,49]. Mutations with any detected
799   mutant reads were considered subclonal if the CCF's 95% confidence interval's upper bound was
800   less than 0.9, and clonal otherwise. This process resulted in 3,507 mutation calls. We next applied
801   a series of filters to exclude mutations which were likely induced by formalin. In addition to only
802   using variants with "PASS" filter status based on GATK *FilterMutectCalls*, we removed SNVs
803   that met all of the following 3 criteria: (1) had the dominant formalin-associated mutation
804   signature[50] C>T (or G>A); (2) were not likely to be oncogenic based on OncoKB annotation; and
805   (3) were detected in only 1 sample, subclonally. We additionally removed any variant for which
806   we suspected the possibility of false negative calls for any sample. Briefly, for every mutation, we
807   checked if any sample that had no reads supporting the mutant allele may have been a false
808   negative due to insufficient power to detect the mutation (e.g., due to insufficient sequencing depth
809   at that position). To this end, we calculated the probability of detecting at least one read with the
810   mutant allele in each sample, given its tumor purity and read depth at that position, and assuming
811   the mutation had a CCF of 20% and arose on one mutant copy. If this probability was below 90%
812   in any sample with 0 mutant reads, we considered this mutation call a potential false negative and
813   therefore removed this mutation from all samples. After applying these filters, 2,385 protein-
814   coding missense, nonsense, splice-site, translation start site mutations, silent mutations, or small
815   in-frame and frame-shift insertions and deletions remained for downstream phylogenetic analyses.
816
817   *Clone detection and phylogeny inference*
818   Mutations that were clonal in at least one sample were clustered into subclones using PyClone-
819   vi[51] and their phylogenetic relationships were inferred using Pairtree[52] and Orchard[53]. Here, we

820   conservatively excluded sample LN2b, as this sample had an unexpectedly large number of

821   variants compared to other samples (3.2x the median number of clonal mutations, 2.7x the median

822   number of variants overall) and was therefore suspicious for being enriched for false positives.

823   (However, LN2b was retained in the overall WES mutation phylogeny). After removing variants

824   that according to Pairtree violate the infinite sites assumption using r*emovegarbage*, we input the

825   remaining variants into PyClone-vi, which was run using a maximum of 20 clones. PyClone-vi

826   identified 7 mutation clusters, which after manual curation to split up clusters with high CCF

827   variance and remove four additional variants with ambiguous clustering resulted in 10 clusters

828   (*i.e.*, clones) comprising 86 mutations. Finally, Orchard was used infer a phylogeny from the 10

829   clones and estimate the proportions of each clone in each tumor sample.

830

831   **Simulated effects of chemotherapy on metastasis heterogeneity**

832   To illustrate the effects of systemic chemotherapy on inter-lesion heterogeneity, we simulated 100

833   patients, each with four high-diversity "peritoneal" lesions and four low diversity "liver" lesions.

834   All lesions initially consisted of 1 million cells that were randomly sampled from 5 subclones (A,

835   B, C, D, E). Peritoneal lesions were created by sampling from each subclone with equal

836   probability, translating into approximately 20% frequency for each clone. Liver lesions were

837   created by sampling from clone A with probability 0.95 and from the remaining clones with

838   probability 0.0125 each. Chemotherapy was then simulated as the random death of 80% of cells

839   in each metastasis. The surviving cells regrew according to a discrete time birth-death process with

840   birth rate 0.25 and death rate 0.24[14] until the lesions contained 100 million cells. At this point,

841   inter-lesion heterogeneities for peritoneal and liver lesions were quantified as the median pair-wise

842   Euclidean distance between lesions of each type.

843

844   **Simulated angular distance between tumors with variable purities**

845   To explore the effects of tumor purity on angular distance, we simulated a phylogeny with two

846   ancestrally related tumor samples of perfect purity. Specifically, we first generated a germline

847   genotype ("c0") which consisted of 100 polyguanine markers of random lengths between 10-20

848   nucleotides. From this germline genotype, we constructed a genotype for the patient's first cancer

849   cell ("c1"): each marker mutated independently with a constant probability of 5×10^{-4} per

850   generation; each mutation was either an insertion or a deletion of 1 basepair with equal probability;

39

851 and 1,000 generations passed between the germline genotype and c1. Next, we simulated two

852 tumor genotypes ("c2" and "c3") that evolved from the ancestral c1 genotype over another 1,000

853 generations. The resulting genotypes c2 and c3 thus represented the genotypes of two 100% pure,

854 ancestrally related tumors. We then numerically admixed the pure tumor genotypes c2 and c3 each

855 with c0 (the germline genotype) at various proportions to create impure tumor genotypes ("t1" and

856 "t2"). The resulting genotypes c0, t1, and t2 represented the *idealized* genotypes of the patient's

857 germline and tumor samples. Technical noise affects measurements from any assay and has a

858 greater effect when the magnitude of the signal is small. We therefore simulate *measured*

859 genotypes by adding random noise to each marker length to represent technical error. As a

860 surrogate measurement for technical noise, we used the precision in marker length measurements.

861 Briefly, for each normal sample in our patient cohort, length distributions for each polyguanine

862 marker were sampled with replacement 200 times, and the coefficient of deviation of their mean

863 lengths (their standard deviation normalized by their mean) was recorded. Across all markers and

864 patients, the median coefficient of variation in marker length was 0.002. Random noise was then

865 simulated with a normal distribution of mean 0 and standard deviation equal to the true length of

866 the marker multiplied by 0.002, and added to every marker length in c0, t1, and t2. Finally, the

867 angular distance between t1 and t2 was calculated (see **Supplementary Note**) using the measured

868 c0 as the genotype of the patient's matched normal sample. This angular distance was then

869 compared to an "optimal" value assuming no technical error and 100% purity of each tumor

870 (**Supplementary Note Fig. 1**).

871

872 **Animal experiments**

873 *Patient-derived organoids and organoid culture.*

874 All human experiments were approved by the ethical committee of University Medical Center

875 Utrecht (UMCU). Written informed consent from the donors for research use of tissue in this study

876 was obtained prior to acquisition of the specimen. Tumor patient-derived organoids (PDOs) were

877 embedded in ice-cold Matrigel® (Corning) mixed with a CRC culture medium in a 3:1 ratio. The

878 medium contained advanced DMEM/F12 medium (Invitrogen), HEPES buffer (Lonza, 10 mM),

879 penicillin/streptomycin (Gibco, 50 U/ml), GlutaMAX (Gibco, 2 mM), R-spondin-conditioned

880 medium (20%), Noggin-conditioned medium (10%), B27 (Thermo/Life Technologies, 1×),

881 nicotinamide (Sigma-Aldrich, 10 mM), N-acetylcysteine (Sigma-Aldrich, 1.25 mM), A83-01

882   (Tocris, 500 nM), EGF (Invitrogen/Life Technologies, 50 ng/ml) and SB202190 (Gentaur, 10 µM).

883   For passaging, the PDOs were dissociated with TrypLE Express (Gibco) for 5–10 min at 37°C and

884   re-plated in a pre-warmed 6-well plate. Rho-associated kinase (ROCK) inhibitor Y-27632 (Tocris,

885   10 µM) was added to culture medium upon plating for two days.

886

887   *Multicolor Marking*

888   The PDOs were simultaneously transduced with three RGB constructs (each encoding for a color)

889   according to a previously published protocol[28]. The following lentiviral gene ontology (LeGO)

890   vectors were used: LeGO-C2 (27339), LeGO-V2 (27340), and LeGO-Cer2 (27338) (Addgene).

891   Briefly, lentiviral production was performed by a calcium phosphate transfection protocol in

892   human embryonic kidney 293T cells using the transfer plasmid (15 µg), pMD2.G (12259, 7.5 µg)

893   and psPAX2 (12260, 7.5 µg). The following day, medium was replaced by advanced DMEM/F12

894   medium (Invitrogen) supplemented with HEPES buffer (Lonza, 10 mM), penicillin/streptomycin

895   (Gibco, 50 U/ml), and GlutaMAX (Gibco, 2 mM). The next day, 50,000 single cells of PDOs were

896   resuspended in the virus medium (which was filtered through 0.45 µm polyethersulfone filter),

897   supplemented with Polybrene (Sigma-Aldrich, 8 µg/ml), N-acetylcysteine (Sigma-Aldrich, 1.25

898   mM) and ROCK-inhibitor Y-27632 (Sigma-Aldrich, 10 µM), and incubated overnight 37°C, 5%

899   (vol/vol) CO_2 on non-adherent plates (ultra-low attachment surface, Sigma-Aldrich). After 24h

900   incubation, cells were washed twice in PBS (Sigma-Aldrich) and cultured as described above. The

901   PDOs were sorted based on YeGr2-A (mCherry), blue 1-A (Venus), and Violet1-A (Cerulean)

902   expression at least two passages after transduction on a Fluorescence Activated Cell Sorting

903   (FACS) Aria II (BD Biosciences) machine.

904

905   *Orthotopic caecum-implantation model*

906   This study was approved by Utrecht University's Animal Welfare Body, the Animal Ethics

907   Committee and licensed by the Central Authority for Scientific Procedures on Animals. To

908   evaluate the spontaneous metastatic capacity of the tumor PDOs, we made use of the murine

909   orthotopic caecum-implantation model[54]. In summary, one day before implantation, RGB-PDOs

910   were dissociated into single cells and 2.5×10^5 cells were plated in 10 µL drops of neutralized Rat

911   Tail High Concentrated Type I Collagen (Corning). The PDOs were allowed to recover overnight

912   at 37°C, 5% (vol/vol) CO_2. NOD.Cg-Prkdc[SCID] Il2rg[tm1Wjl]/SzJ (NSG) male mice, between 8-10

41

913   weeks of age, were treated with a subcutaneous dose of analgesic Carprofen (5 mg/kg, Rimadyl^{TM})

914   30 min before surgery and were subsequently sedated by isoflurane inhalation anesthesia [2%

915   (vol/vol) isoflurane/O2 mixture]. The caecum was exteriorized through a midline abdominal

916   incision and a single collagen drop containing the RGB-PDOs was micro-surgically transplanted

917   in the cecal submucosa. Carprofen was given 24h post-surgery. The endpoint for all animals

918   reached after five weeks. Caecum, liver and peritoneum were harvested for further analysis.

919

920   *Tissue processing and image analysis*

921   Mouse organs containing multicolor, endogenously fluorescent primary tumors and metastases

922   were fixed using 4%-paraformaldehyde in PBS solution overnight at 4°C followed by tissue

923   preservation in a 20% sucrose solution for 12h at 4°C. Samples were cut into 4 μm-thick frozen

924   tissue sections and covered with ProLong Gold Antifade Mountant (Thermo Fisher Scientific). For

925   high-resolution imaging, sections were scanned with an LSM 700 confocal microscope (Carl

926   Zeiss) using an EC Plan-Neofluar 10x/0.30 or 20x/0.50 M27 objective. Fluorescence images were

927   preprocessed by downsampling to 1.25 μm/pixel and Gaussian filtering (scikit-image, scipy-

928   ndimage, Python). For all images and image channels, auto-fluorescence of the background tissue

929   was individually contrast corrected by intensity clipping at appropriate, manually chosen,

930   thresholds (**Supplementary Table 6**) followed by rescaling pixel values to 0.6% oversaturation.

931   Lesions were manually highlighted as regions of interest (Labkit, Fiji) and images were split into

932   separate images for each lesion. Pixel values were filtered for pixels in which the sum of RGB

933   values was at least 50 and converted to the HSV scale. For each image, Hue values were binned

934   into 10 equally sized bins and counted before calculating the Simpson diversity index (*vegan*, R)

935   (approach adapted from Coffey et al.[55]). The average diversity was calculated over a total of 10

936   repetitions, each time shifting the bin positions. Differences in SDI values between caecum,

937   peritoneum, and liver regions were assessed using a Kruskal-Wallis test followed by Dunn's test

938   with Holm's correction for multiple hypothesis testing.

939

940   **Statistical analyses and figures**

941   All statistical analyses were performed with R (version 4.1.1) unless otherwise noted. In boxplots

942   comparing two groups, statistical differences were tested with unpaired two-sided Wilcoxon rank

943   sum tests and effect sizes were calculated using the *rstatix* R library. For boxplots with pairwise-

944 comparisons of three or more groups, a Kruskal-Wallace test was used followed by a post-hoc

945 Dunn's test with Holm's correction for multiple hypothesis testing as implemented in the *rstatix*

946 library, and Wilcoxon rank sum test effect sizes are provided for each comparison. *p*-values from

947 independent tests were corrected for multiple hypothesis testing with the Benjamini-Hochberg

948 method and reported as *q*-values method where appropriate. In all boxplots, boxes show the

949 median value with lower and upper hinges corresponding to the 25th and 75th percentile values,

950 respectively. Boxplot whiskers extend from the lower/upper hinges to the smallest/largest values

951 no further away than 1.5 times the inter-quartile range from the hinge. Figures were generated with

952 either base-R or the *ggplot2* library. Phylogenetic trees were visualized using the *ggtree* library[56].

953

954 **Data availability**

955 Easily machine readable raw polyguanine marker data are available at

956 https://github.com/agorelick/peritoneal_metastasis. Processed data files used as input for analyses

957 in this study, including angular distance matrices, lpWGS binned read counts and full clinical data

958 are available at the same repository. As for all our previous studies, the raw data has also been

959 submitted to Data Dryad and is ready to download for reviewers under:

960 https://datadryad.org/stash/share/jYnd55JoQ5F6gRYI0LwHd3RZ83TQv7W3jFGN-B0bts0.

961 Deposition of raw lpWGS and whole exome sequencing data to dbGAP has been initiated; the full

962 data set will be available at the time of publication (preliminary accession ID: phs003722.v1.p1).

963

964 **Code availability**

965 Code and instructions to regenerate all data-based figures is available at

966 https://github.com/agorelick/peritoneal_metastasis. Angular distance matrices can be regenerated

967 from marker files by running the complete polyguanine PCR assay data-processing pipeline, which

968 is available at https://github.com/agorelick/polyG.

969

970 **Acknowledgements**

976

977

Competing financial interests

979   The authors declare no competing financial interests.

980

981

References

983

984   1.   Al Bakir, M. *et al.* The evolution of non-small cell lung cancer metastases in TRACERx.

985   *Nature* **616**, 534–542 (2023).

986   2.   Turajlic, S. *et al.* Tracking Cancer Evolution Reveals Constrained Routes to Metastases:

987   TRACERx Renal. *Cell* **173**, 581-594.e12 (2018).

988   3.   McPherson, A. *et al.* Divergent modes of clonal spread and intraperitoneal mixing in high-

989   grade serous ovarian cancer. *Nat. Genet.* **48**, 758–767 (2016).

990   4.   Gundem, G. *et al.* The evolutionary history of lethal metastatic prostate cancer. *Nature* **520**,

991   353–357 (2015).

992   5.   Hu, Z. *et al.* Quantitative evidence for early metastatic seeding in colorectal cancer. *Nat.*

993   *Genet.* **51**, 1113–1122 (2019).

994   6.   Weinberg, R. A. Mechanisms of malignant progression. *Carcinogenesis* **29**, 1092–1095

995   (2008).

996   7.   Fidler, I. J. & Kripke, M. L. Metastasis results from preexisting variant cells within a

997   malignant tumor. *Science* **197**, 893–895 (1977).

998   8.   Minn, A. J. *et al.* Genes that mediate breast cancer metastasis to lung. *Nature* **436**, 518–524

999   (2005).

1000   9.   Reiter, J. G. *et al.* Minimal functional driver gene heterogeneity among untreated metastases.

1001   *Science* **361**, 1033–1037 (2018).

1002   10. Patel, S. A., Rodrigues, P., Wesolowski, L. & Vanharanta, S. Genomic control of metastasis.

1003   *Br. J. Cancer* **124**, 3–12 (2021).

1004   11.   Gymrek, M., McGuire, A. L., Golan, D., Halperin, E. & Erlich, Y. Identifying personal
1005   genomes by surname inference. *Science* **339**, 321–324 (2013).

1006   12.   Naxerova, K. *et al.* Hypermutable DNA chronicles the evolution of human colon cancer.
1007   *Proc. Natl. Acad. Sci. U. S. A.* **111**, E1889-98 (2014).

1008   13.   Naxerova, K. *et al.* Origins of lymphatic and distant metastases in human colorectal cancer.
1009   *Science* **357**, 55–60 (2017).

1010   14.   Reiter, J. G. *et al.* Lymph node metastases develop through a wider evolutionary bottleneck
1011   than distant metastases. *Nat. Genet.* **52**, 692–700 (2020).

1012   15.   Blohmer, M. *et al.* Quantifying cell divisions along evolutionary lineages in cancer. Preprint
1013   available at ResearchSquare. https://doi.org/10.21203/rs.3.rs-3839927/v1 (2024).

1014   16.   Ubellacker, J. M. *et al.* Lymph protects metastasizing melanoma cells from ferroptosis.
1015   *Nature* **585**, 113–118 (2020).

1016   17.   Sleeman, J. P. The lymph node as a bridgehead in the metastatic dissemination of tumors. in
1017   *Recent Results in Cancer Research* vol. 157 55–81 (Springer Berlin Heidelberg, Berlin,
1018   Heidelberg, 2000).

1019   18.   Lurvink, R. J. *et al.* Increase in the incidence of synchronous and metachronous peritoneal
1020   metastases in patients with colorectal cancer: A nationwide study. *Eur. J. Surg. Oncol.* **47**,
1021   1026–1033 (2021).

1022   19.   Franko, J. *et al.* Prognosis of patients with peritoneal metastatic colorectal cancer given
1023   systemic therapy: an analysis of individual patient data from prospective randomised trials
1024   from the Analysis and Research in Cancers of the Digestive System (ARCAD) database.
1025   *Lancet Oncol.* **17**, 1709–1719 (2016).

1026   20.   Lenos, K. J. *et al.* Molecular characterization of colorectal cancer related peritoneal metastatic
1027   disease. *Nat. Commun.* **13**, 4443 (2022).

1028   21.   Laoukili, J. *et al.* Peritoneal metastases from colorectal cancer belong to Consensus Molecular
1029   Subtype 4 and are sensitised to oxaliplatin by inhibiting reducing capacity. *Br. J. Cancer* **126**,
1030   1824–1833 (2022).

1031   22.   Ubink, I. *et al.* Histopathological and molecular classification of colorectal cancer and
1032   corresponding peritoneal metastases. *Br. J. Surg.* **105**, e204–e211 (2018).

23. Estabrook, G. F., McMorris, F. R. & Meacham, C. A. Comparison of Undirected Phylogenetic Trees Based on Subtrees of Four Evolutionary Units. *Syst. Zool.* **34**, 193–200 (1985).

24. Shibata, D., Navidi, W., Salovaara, R., Li, Z. H. & Aaltonen, L. A. Somatic microsatellite mutations as molecular tumor clocks. *Nat. Med.* **2**, 676–681 (1996).

25. Bootsma, S., Bijlsma, M. F. & Vermeulen, L. The molecular biology of peritoneal metastatic disease. *EMBO Mol. Med.* **15**, e15914 (2023).

26. Cortés-Guiral, D. *et al.* Primary and metastatic peritoneal surface malignancies. *Nat Rev Dis Primers* **7**, 91 (2021).

27. Kreso, A. *et al.* Variable clonal repopulation dynamics influence chemotherapy response in colorectal cancer. *Science* **339**, 543–548 (2013).

28. Weber, K., Thomaschewski, M., Benten, D. & Fehse, B. RGB marking with lentiviral vectors for multicolor clonal cell tracking. *Nat. Protoc.* **7**, 839–849 (2012).

29. Oosterling, S. J., van der Bij, G. J., van Egmond, M. & van der Sijp, J. R. M. Surgical trauma and peritoneal recurrence of colorectal carcinoma. *Eur. J. Surg. Oncol.* **31**, 29–37 (2005).

30. Lemmens, V. E. *et al.* Predictors and survival of synchronous peritoneal carcinomatosis of colorectal origin: a population-based study. *Int. J. Cancer* **128**, 2717–2725 (2011).

31. Zhang, C. *et al.* Mapping the spreading routes of lymphatic metastases in human colorectal cancer. *Nat. Commun.* **11**, 1–11 (2020).

32. Dieterich, L. C., Tacconi, C., Ducoli, L. & Detmar, M. Lymphatic vessels in cancer. *Physiol. Rev.* **102**, 1837–1879 (2022).

33. Jain, R. K., Martin, J. D. & Stylianopoulos, T. The role of mechanical forces in tumor growth and therapy. *Annu. Rev. Biomed. Eng.* **16**, 321–346 (2014).

34. Kim, T.-M. *et al.* Subclonal genomic architectures of primary and metastatic colorectal cancer based on intratumoral genetic heterogeneity. *Clin. Cancer Res.* **21**, 4461–4472 (2015).

35. Nagtegaal, I. D. *et al.* Tumor deposits in Colorectal cancer: Improving the value of modern staging-A systematic review and meta-analysis. *J. Clin. Oncol.* **35**, 1119–1127 (2017).

36. Österreicher, F. & Vajda, I. A new class of metric divergences on probability spaces and its applicability in statistics. *Ann. Inst. Stat. Math.* **55**, 639–653 (2003).

37. Paradis, E., Claude, J. & Strimmer, K. APE: Analyses of Phylogenetics and Evolution in R language. *Bioinformatics* **20**, 289–290 (2004).

1064   38. Babraham Bioinformatics - FastQC A Quality Control tool for High Throughput Sequence
1065   Data. https://www.bioinformatics.babraham.ac.uk/projects/fastqc/.

1066   39. Li, H. Aligning sequence reads, clone sequences and assembly contigs with BWA-MEM.
1067   *arXiv [q-bio.GN]* (2013).

1068   40. Scheinin, I. *et al.* DNA copy number analysis of fresh and formalin-fixed specimens by
1069   shallow whole-genome sequencing with identification and exclusion of problematic regions
1070   in the genome assembly. *Genome Res.* **24**, 2022–2032 (2014).

1071   41. Poell, J. B. *et al.* ACE: absolute copy number estimation from low-coverage whole-genome
1072   sequencing data. *Bioinformatics* **35**, 2847–2849 (2019).

1073   42. Sand, A. *et al.* tqDist: a library for computing the quartet and triplet distances between binary
1074   or general trees. *Bioinformatics* **30**, 2079–2080 (2014).

1075   43. Martin, M. Cutadapt removes adapter sequences from high-throughput sequencing reads.
1076   *EMBnet J.* **17**, 10 (2011).

1077   44. DePristo, M. A. *et al.* A framework for variation discovery and genotyping using next-
1078   generation DNA sequencing data. *Nat. Genet.* **43**, 491–498 (2011).

1079   45. Karczewski, K. J. *et al.* The mutational constraint spectrum quantified from variation in
1080   141,456 humans. *Nature* **581**, 434–443 (2020).

1081   46. Suehnholz, S. P. *et al.* Quantifying the expanding landscape of clinical actionability for
1082   patients with cancer. *Cancer Discov.* **14**, 49–65 (2024).

1083   47. Shen, R. & Seshan, V. E. FACETS: allele-specific copy number and clonal heterogeneity
1084   analysis tool for high-throughput DNA sequencing. *Nucleic Acids Res.* **44**, e131 (2016).

1085   48. McGranahan, N. *et al.* Clonal status of actionable driver events and the timing of mutational
1086   processes in cancer evolution. *Sci. Transl. Med.* **7**, 283ra54 (2015).

1087   49. Dentro, S. C., Wedge, D. C. & Van Loo, P. Principles of reconstructing the subclonal
1088   architecture of cancers. *Cold Spring Harb. Perspect. Med.* **7**, (2017).

1089   50. Guo, Q. *et al.* The mutational signatures of formalin fixation on the human genome. *Nat.*
1090   *Commun.* **13**, 4487 (2022).

1091   51. Gillis, S. & Roth, A. PyClone-VI: scalable inference of clonal population structures using
1092   whole genome data. *BMC Bioinformatics* **21**, 571 (2020).

1093   52. Wintersinger, J. A. *et al.* Reconstructing complex cancer evolutionary histories from multiple
1094   bulk DNA samples using Pairtree. *Blood Cancer Discov.* **3**, 208–219 (2022).

1095   53.   Kulman, E., Kuang, R. & Morris, Q. Orchard: building large cancer phylogenies using
1096   stochastic combinatorial search. *arXiv [q-bio.PE]* (2023).

1097   54.   Fumagalli, A. *et al.* A surgical orthotopic organoid transplantation approach in mice to
1098   visualize and study colorectal cancer progression. *Nat. Protoc.* **13**, 235–247 (2018).

1099   55.   Coffey, S. E., Giedt, R. J. & Weissleder, R. Automated analysis of clonal cancer cells by
1100   intravital imaging. *Intravital* **2**, e26138 (2013).

1101   56.   Yu, G. Using ggtree to Visualize Data on Tree-Like Structures. *Curr. Protoc. Bioinformatics*
1102   **69**, e96 (2020).

1103

1104